Received: 8 April 2022 | Revised: 17 November 2022 | Accepted: 18 November 2022 | Published on: 3 January 2023

DOI: 10.1002/qj.4407

Quarterly Journal of the Royal Meteorological Society RMetS

RESEARCH ARTICLE

Sources of anisotropy in the Reynolds stress tensor in the stable boundary layer

Federica Gucci[1] | **Lorenzo Giovannini**[1] | **Ivana Stiperski**[2] | **Dino Zardi**[1] | **Nikki Vercauteren**[3]

[1]Department of Civil, Environmental and Mechanical Engineering, University of Trento, Trento, Italy

[2]Department of Atmospheric and Cryospheric Sciences, University of Innsbruck, Innsbruck, Austria

[3]Department of Geosciences, University of Oslo, Oslo, Norway

Correspondence
F. Gucci, Department of Civil, Environmental and Mechanical Engineering, University of Trento, Trento 38122, Italy.
Email: federica.gucci@unitn.it
N. Vercauteren, Department of Geosciences, University of Oslo, Oslo, Norway.
Email: nikki.vercauteren@geo.uio.no

Abstract

Data collected by 12 sonic anemometers over the Plaine Morte Glacier (Swiss Alps) during the Snow Horizontal Arrays Turbulence Study are used to investigate sources of anisotropy in the Reynolds stress tensor for stable boundary layers. A coarse-graining approach is applied to evaluate transfers of kinetic energy across scales, and internal gravity waves (IGWs) are detected with a suitable criterion. Both approaches are combined with a classification of anisotropy based on the barycentric map of 1 min Reynolds stress tensors. A wind-speed threshold is found that discriminates between regimes with a different dominant topology of the Reynolds stress tensor. One-component and isotropic states are frequent for low wind speed and strong stratification, whereas two-component axisymmetric states dominate the high wind speed regime with strong vertical shear. Results suggest that the presence of IGWs is mostly responsible for one-component states, and additionally influences the relative amount of kinetic and potential energy in the perturbation field. To provide supporting evidence, a complementary analysis of a clean IGW detected during a field campaign in Dumosa (Australia) is presented. This case study highlights how waves contribute to drive the Reynolds stress tensor towards the one-component limit. Cases are shown where a linear detrending procedure may be effective in filtering out waves and avoid their spurious contributions in turbulence statistics.

KEYWORDS

anisotropy, internal waves, inverse cascade, linear detrending, stable boundary layer, stratified turbulence, wind speed threshold

1 | INTRODUCTION

Under a variety of meteorological conditions, the planetary boundary layer (PBL) is characterised by stable stratification. It may develop due to significant radiative cooling of the surface during night-time under clear sky, or due to advection or subsidence of warm air masses over cold seas or ice, as frequently found in polar regions.

Despite its relevance for various environmental hazards of societal importance, such as high concentrations of pollutants and frost and fog formation, a comprehensive understanding of all the processes involved in the stable boundary layer (SBL) is still missing. This is particularly true for very stable conditions, for which turbulence dynamics is hard to predict. In those conditions, turbulence is non-stationary, it strongly interacts with small-scale non-turbulent motions that may have propagated over long distances, and there is a strong interplay between velocity fluctuations and stratification.

Recent contributions focused on identifying different dynamic regimes in the SBL and attempted to parametrise turbulence accordingly. In particular, a classification of the SBL in two dynamic regimes depending on the wind speed was proposed by Sun *et al.* (2012) and then verified by many experimental (Mahrt *et al.*, 2015; Vignon *et al.*, 2017; Acevedo *et al.*, 2021) and numerical studies (Baas *et al.*, 2019; Maroneze *et al.*, 2019a; Maroneze *et al.*, 2019b). A site- and height-dependent wind-speed threshold was found to discriminate between an SBL "decoupled regime" (where turbulence is weak, intermittent, mainly controlled by the local shear, and does not directly interact with the ground – low wind-speed cases) and a "coupled regime" (where turbulence is strong, continuous, and controlled by the bulk shear – high wind-speed cases). As eddies detach from the ground, the Monin–Obukhov similarity theory predicts that z is no longer a scaling parameter and turbulence follows z-less scaling in the decoupled state. However, in very stable conditions, the decoupled state exhibits departures even from this ad-hoc theory. On the other hand, Monin–Obukhov similarity theory was shown to work well for experimental data with close to isotropic Reynolds stress tensors (Stiperski and Calaf, 2018), which implies an equal contribution from the three velocity components of the turbulent kinetic energy (TKE) and experimental data following the −5/3 Kolmogorov power law in the inertial subrange (Grachev *et al.*, 2013).

For very stable stratification, the Reynolds stress tensor is far from isotropic. In fact, a large-eddy simulation (LES) (Ali *et al.*, 2018) has shown that the most remarkable difference between unstable, neutral, and stable atmospheric conditions is the tendency of turbulent stresses for stable stratification to be characterised by velocity fluctuations along one dominant direction in the coordinate system made of the tensor's eigenvectors. This state of anisotropy of the Reynolds stress tensor is called one-component turbulence (Pope, 2000, table 11.1). Analogous results were found by Falocchi *et al.* (2019) analysing the dependence of turbulence anisotropy on wind intensity and atmospheric stability.

Moreover, for very stable stratification, turbulence does not satisfy the assumptions implied in the derivation of the −5/3 power law (Kolmogorov, 1941). In fact, Kolmogorov theory for the inertial subrange is valid only in neutral conditions and follows from the assumption of a universal character (independent of the flow geometry) of small-scale turbulent motions, determined entirely by the rate at which they receive kinetic energy from the large scales and dissipate it into heat through viscosity. Turbulence in a stable atmosphere is strongly influenced by density stratification, which leads to a viscous dissipation rate that is significantly smaller than the rate of generation of TKE, as part of it is converted into potential energy and smoothed out by molecular conductivity (Bolgiano, 1959; Finnigan *et al.*, 1984; Zilitinkevich *et al.*, 2019). For sufficiently stable stratification, the inertial subrange in the vertical spectra of the horizontal velocity may even disappear (Lang and Waite, 2019) and the entire spectrum is anisotropic (Bolgiano, 1959). Nevertheless, most of the parametrisations for PBL turbulence, both in Reynolds averaged Navier–Stokes (RANS) simulations and in LESs, assume local isotropy for the smallest eddies in order to parametrise the dissipation tensor, which is then computed parametrising only one out of nine terms. RANS simulations generally use closures up to order 1.5, including a TKE budget equation with viscous dissipation parametrised according to Kolmogorov's law, $\varepsilon \propto u^3 l^{-1}$ (Pope, 2000; Vassilicos, 2015). The most common LES models are based on the assumption that the filtering scale is in the inertial subrange and that large-scale anisotropic eddies are fully resolved. The unresolved motions are hence expected to be locally homogeneous and isotropic and are parametrised accordingly.

A proper representation of the SBL needs an improvement of the classical theories adopted so far to describe boundary-layer flows. This, in turn, requires a better understanding of the physical processes that cause deviations of turbulence properties from classical theories. In particular, the physical processes leading to turbulence anisotropy will be investigated here.

Sources of anisotropy for eddy motion in the inertial subrange have been investigated by direct numerical simulations (DNSs) (Smyth and Moum, 2000; Lang and Waite, 2019; Kit *et al.*, 2021), laboratory experiments (Atta, 1991), and field studies (Kit *et al.*, 2021). Results suggest that departures from local isotropy may occur because of interactions between the temperature and velocity fields at small scales and direct interactions between the large-scale and small-scale eddy motions (Katul *et al.*, 1995). Considering anisotropy at larger turbulent scales, Stiperski and Calaf (2018) found that the horizontal velocity spectrum of one-component turbulence has a spectral slope of −2.4 in the low-frequency range, and they pointed out that the value is close to a −3 slope, characteristic of both turbulence, when constrained to a quasi-two-dimensional flow, and the canonical gravity wave spectrum, derived from strong nonlinear interactions between turbulence and internal gravity waves (IGWs) (Sukoriansky and Galperin, 2012). Following up on that study, Vercauteren *et al.* (2019a) showed that one-component turbulence occurred when submeso-scale motions and turbulent scales overlapped.

In this paper we explore the hypothesis that strong temperature stratifications, such as those occurring over glaciers and typical of the decoupled SBL where one-component turbulence dominates, attenuate turbulent vertical motions enough to enable the development of quasi-two-dimensional dynamics. In such quasi-two-dimensional dynamics, the vortex stretching term is null and the conservation of enstrophy, as well as energy conservation, prevent the downscale cascade of energy. In the spectral range below the forcing wave number, the transfer of energy is towards the large scales (backscatter), leading to an inverse cascade (Vallis, 2005, sec. 8.3). The organisation of the flow into horizontal layers of eddies separated by strong vertical shear, with the formation of horizontal pancake-like structures in physical space – classified as two-dimensional modes by Mahrt (2014) – has already been observed, combined with a tendency of energy to accumulate in the vertical conical region in Fourier space (Sagaut and Cambon, 2018, fig. 10.5) for increasing stratification (Sukoriansky and Galperin, 2012). Since a −3 slope with an inverse cascade of energy is usually found in the synoptic range of the energy spectrum, where large-scale flows are constrained by Earth rotation and stratification, we are also indirectly wondering if phenomena generally attributed to large-scale dynamics might also occur at smaller scales. For example, by solving the two-dimensional RANS equations numerically and analytically under the assumptions of constant horizontal gradients of wind velocity components and pressure and by neglecting the horizontal gradients of the Reynolds stresses (Oettl *et al.*, 2005), it has been shown that meandering (a phenomenon occurring at low wind speed in the boundary layer and related to the horizontal oscillations of the wind direction) is an inherent property of the flow when it approaches the geostrophic balance, which is usually attributed to large-scale dynamics. Our hypothesis was also motivated by theories (Schertzer and Lovejoy, 1985; Lovejoy *et al.*, 1993; Lovejoy and Schertzer, 2013) suggesting that there is no spectral gap or a strict separation between two- and three-dimensional atmospheric motions: small-scale structures are continuously deformed and flattened at larger and larger scales by a scale-invariant process, and scaling methods with anisotropic cascades should be proposed.

In large-scale dynamics, both potential energy and kinetic energy need to be included in modelling eddy motions, and the importance of the energy exchanges between them is well known. This concept was also introduced for boundary-layer flows in a stably stratified atmosphere (Zilitinkevich *et al.*, 2007). By properly scaling the equation for temperature variance to have a prognostic equation for turbulent potential energy (TPE), it becomes apparent that the buoyancy term involving vertical heat fluxes may transfer energy between the potential energy reservoir and the kinetic energy of the turbulent field, as the same term appears with opposite sign in the TKE equation. One-dimensional RANS simulations highlight the importance of this energy exchange mechanism for resolving the transition between the coupled and decoupled regimes of the SBL. By comparing results from models with an increasing number of prognostic equations for turbulent variables, Maroneze *et al.* (2019a) showed that the weak-wind regime can be properly reproduced only if the vertical heat flux and the temperature variance are solved by prognostic equations. Further investigations with a second-order closure numerical model (without prognostic equations for the horizontal momentum flux and the vertical velocity variance) have shown that the vertical heat flux controls the transition between the coupled and decoupled regimes of the SBL, despite its small magnitude (Maroneze *et al.*, 2019b).

An important source of temperature fluctuations at low frequencies in strongly stratified flows are IGWs. Stiperski and Calaf (2018) proposed IGWs as the other possible cause to explain the spectral slope found in the low-frequency range of one-component Reynolds stresses, in agreement with the spectral transition from −3 to −5/3 observed at the Ozmidov wave number in strongly stratified flows (Alisse and Sidi, 2000; Sukoriansky and Galperin, 2012; Lang and Waite, 2019). Thus, the second hypothesis that we explore in this paper is whether IGWs are related to the occurrence of Reynolds stresses towards the one-component limit, also at smaller scales. More generally, it has been shown that submeso motions (such as wave-like motions, gravity currents, or vortical structures between the mesoscale and the largest turbulent eddies) may trigger turbulence events in the most stable regime with a Richardson number above the critical value 0.25 and affect vertical velocity fluctuations at small scales (Vercauteren and Klein, 2015; Vercauteren *et al.*, 2016). The lack of a spectral energy gap in the SBL between the submeso scales and the turbulence in the case of strong submeso activity and the relation with a Reynolds stress tensor towards the one-component limit have been recently pointed out by Vercauteren *et al.* (2019a) with a statistical clustering technique. DNSs of turbulence resulting from Kelvin–Helmholtz instability in stably stratified shear flow indicate that one-component eddies are mainly present in the decay phase of the disturbance (Smyth and Moum, 2000; Wingstedt *et al.*, 2015), and some researchers associate that with jet-like motions (Wingstedt *et al.*, 2015). By performing an analogous DNS but in a very large computational domain, Watanabe *et al.* (2019) attested the formation of highly elongated structures with positive and negative streamwise velocity fluctuations, and Watanabe and Nagata (2021) showed that their contribution to the Reynolds stress tensor is towards the one-component limit. A DNS including the effect of rotation, which corresponds to the stably stratified Ekman flow, also revealed elongated streaky regions (slow-moving fluid) close to the wall (Harikrishnan *et al.*, 2021). Laboratory experiments performed in wave flumes (Longo *et al.*, 2017; Singh *et al.*, 2021) found evidence that one-component eddies are related to surface waves superimposed over steady currents, suggesting that the modulation of the flow at lower frequencies may alter turbulence fluctuations at higher frequency.

Thus, the main questions that will be addressed in this paper are as follows: How are the coupled and decoupled regimes of the SBL related to the anisotropy of the Reynolds stress tensor at small scales? Are the mechanisms of exchange of energy in a one-component limiting state similar to those in quasi-two-dimensional flows, both in large-/small-scale energy transfer and in TKE/TPE transfer? Is there a relation between IGWs and the anisotropy of the Reynolds stress tensor? We address these questions by analysing data from the Snow Horizontal Array Turbulence Study (SnoHATS) dataset, which is described in Section 2. Section 3 introduces the invariant decomposition to study the anisotropic properties of the Reynolds stress tensor, together with a filtering approach to investigate energy transfers across scales, and a diagnostic method for IGWs detection based on cross-spectral analysis. Results are then presented and discussed in Section 4, and conclusions are drawn in Section 5.

2 | OBSERVATIONS

The analysis performed in this paper is based on field measurements from the SnoHATS experimental campaign (Bou-Zeid *et al.*, 2010). The dataset was collected over the Plaine Morte Glacier in the Swiss Alps (46.38638° N, 7.51788° E, 2,750 m a.s.l., Figure 1a) from February 2 to April 19, 2006, and the instruments' set-up was originally designed to study small-scale turbulence in the stable atmospheric surface layer and related parametrisations in LES. Twelve sonic anemometers (sampling frequency 20 Hz) were deployed for the campaign, arranged in two vertically separated horizontal arrays with five sonics in the top layer and seven in the bottom layer (Figure 1b), in order to allow for computation of the full three-dimensional gradients of the measured fields. The separation between neighbouring sonics was 0.80 m in the horizontal and 0.77 m in the vertical direction for data collected until March 14, then the vertical distance was increased to 0.82 m. The height of the instruments above ground level (a.g.l.) changed according to snow cover on the surface of the glacier, with the bottom array at a height between 0.62 m and 2.92 m above snow level. Sonic anemometers pointed to the east, and data analysis was restricted to winds blowing from ±60° with respect to this direction. This ensures that the instruments are in the

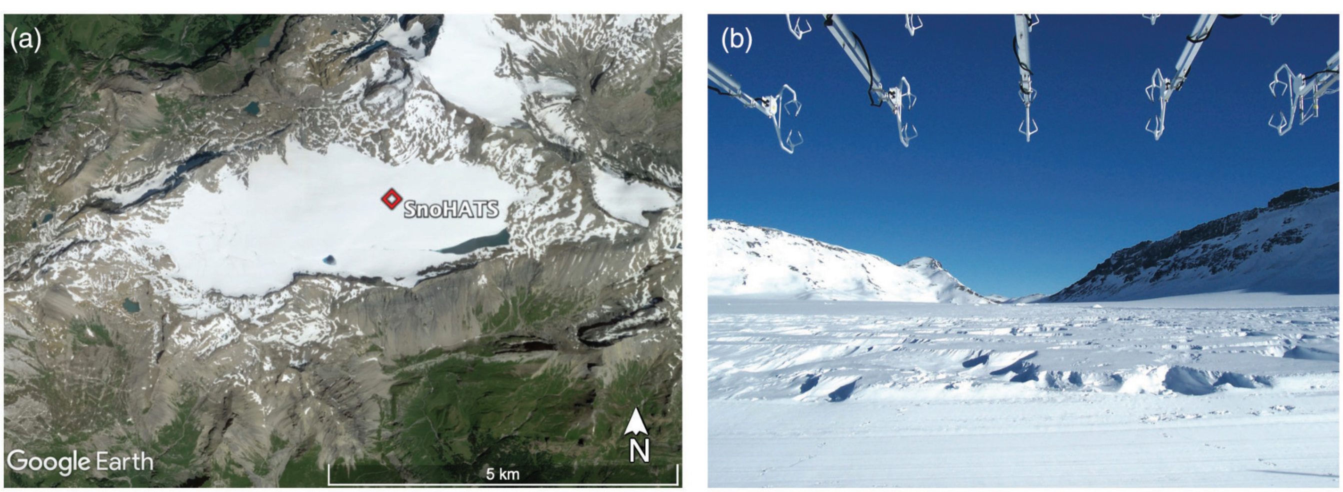

FIGURE 1 Experimental site of the field campaign Snow Horizontal Array Turbulence Study. (a) The location of the sonic anemometers on an aerial photograph of the Plaine Morte Glacier (background map from Google Earth). (b) The two arrays of sonic anemometers, pointing in the east direction [Colour figure can be viewed at wileyonlinelibrary.com]

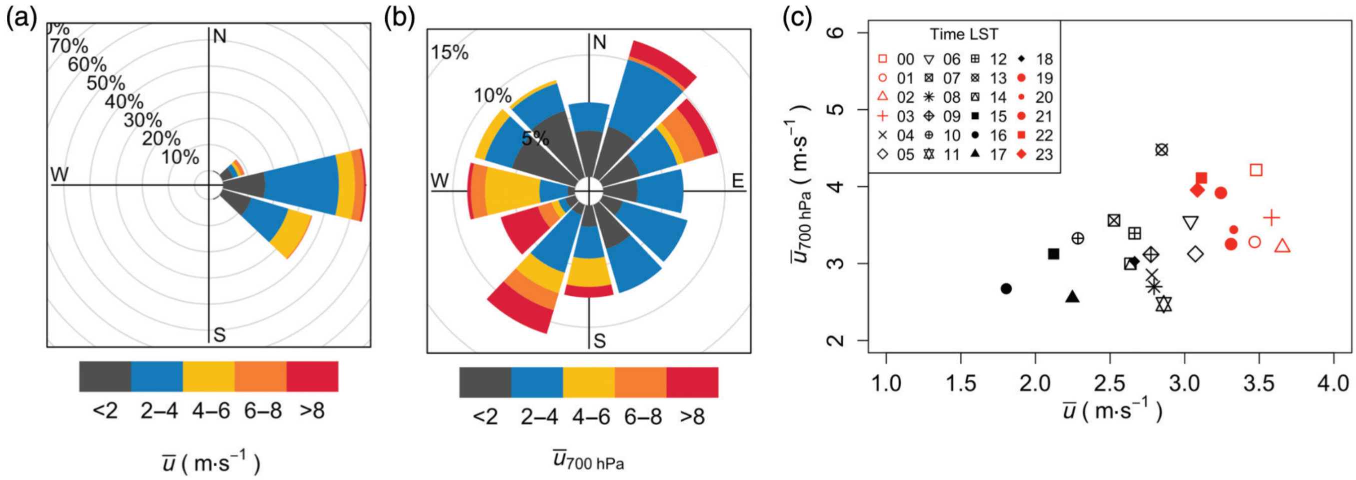

FIGURE 2 Hourly wind roses from Snow Horizontal Array Turbulence Study (SnoHATS) measurements and the ERA5 dataset. (a) The wind rose computed by collecting hourly averages from all the sonic anemometers, based on ~ 1 min windows selected for data analysis. (b) The wind rose based on ERA5 hourly averages, at 700 hPa at the geographical point closest to the SnoHATS location. Both wind roses include only hours corresponding to periods with at least 50% of ~ 1 min windows selected for data analysis. (c) Comparison of the hourly wind speeds, averaged according to the hour of the day (LST: local sidereal time) [Colour figure can be viewed at wileyonlinelibrary.com]

internal equilibrium layer, because winds are blowing over a long fetch of flat snow (Figure 1b, ~ 1,500 m). Additionally, easterly winds at the field site are typically dry and associated with days of clear sky, low-synoptic forcing conditions, and no precipitation (Bou-Zeid *et al.*, 2010), thus ensuring the best operating conditions for the instruments. Low-quality data (including snow-covered sonics, power outages, and other instrumental issues) were removed, thus leaving non-continuous periods equivalent to 14 × 24 hr of data for the analysis. The data selected were collected under weak synoptic forcing conditions, as shown in Figure 2b by the wind rose referring to the standard isobaric level closest to the measurement altitude (700 hPa) at the geographical point closest to the SnoHATS location. The wind rose is obtained from hourly data from the ERA5 reanalysis, provided by the European Centre for Medium-Range Weather Forecasts, including only hours corresponding to periods with at least 50% of 1 min windows selected for data analysis. Wind speed at 700 hPa is mainly below 6 m·s^{-1} and without any preferred direction, highlighting that the selected observed easterly winds (Figure 2a) are decoupled from large-scale motion. On the other hand, the observed easterly winds might be associated with thermally driven local flows. Indeed, the upwind fetch has a gently rising inclination (~2°), ending with a ridgeline, which might drive thermally driven katabatic winds. Figure 2c compares hourly wind speeds at 700 hPa with those measured by the sonics, averaged according to the hour of the day. The latter were obtained by computing hourly averages from ~1 min periods, including only hours with at least 50% of periods selected for data analysis. The length of the data periods was chosen consistently with the turbulence analysis, as will be explained in Section 3.1.1. This comparison confirms that the measured wind speed, which exhibits low variability, is not influenced by the synoptic wind. On the other hand, stronger wind speeds are clearly characterizing night-time hours, as shown in Figure 2c, thus supporting the hypothesis that topography contributes to the development of stronger easterly winds during night-time.

To evaluate turbulent quantities, previous analyses of the co-spectral gap (Vercauteren *et al.*, 2016) suggested 1 min averaging windows, which should minimise the contamination from non-turbulent motions for weak-wind stable conditions. This time window is also used in this paper. Data were processed using double rotation and applying linear detrending. The influence of the latter procedure on evaluating the state of turbulence anisotropy will be discussed in Section 3.1.1. The anisotropy analysis is based on quantities that are invariant to the coordinate system; hence, the double rotation has no influence on the results. Where the planar-fit technique is used for data analysis, attention should be paid to a possible influence on the results, but this method is not used in this paper.

3 | METHODS

3.1 | Anisotropy of the Reynolds stress tensor

The Reynolds stress tensor is a (symmetric) second-order three-dimensioanl tensor (positive semi-definite); as such, it may be decomposed into an isotropic and an anisotropic deviatoric (trace-free) part:

$$\overline{u_i' u_j'} = \frac{2k}{3}\delta_{ij} + a_{ij}, \tag{1}$$

where u_i' are velocity fluctuations with respect to a time average, denoted by an overbar, δ_{ij} is the Kronecker delta, and $k = \frac{1}{2}(\overline{u_1'^2} + \overline{u_2'^2} + \overline{u_3'^2})$ is the TKE. The TKE is half the trace of the Reynolds stress tensor; and since the trace is the first principal invariant of a tensor, TKE does not depend on the frame of reference in which velocity fluctuations are measured. Only the deviatoric part a_{ij} is effective in transporting momentum, while the isotropic stresses can be simply absorbed in a modified mean-pressure term. The analysis of the normalised anisotropic Reynolds stress tensor

$$b_{ij} = \frac{a_{ij}}{2k} = \frac{\overline{u_i' u_j'}}{2k} - \frac{1}{3}\delta_{ij} \tag{2}$$

has recently received increasing attention to improve turbulence parametrisations in the atmospheric surface layer (Stiperski and Calaf, 2018) or to develop new methodologies for uncertainty quantification of turbulence closures in RANS or LES approaches (Emory *et al.*, 2013; Jofre *et al.*, 2018; Mishra *et al.*, 2020). The symmetry of b_{ij} ensures diagonalisability of the matrix, whose components in the diagonal form in the principal coordinate system (pcs) are the three matrix's eigenvalues, λ_1, λ_2, and λ_3, with $\lambda_1 \geq \lambda_2 \geq \lambda_3$, which are real and can be computed by built-in functions in different programming languages (such as the *eigen()* function in the R language). The sum of the three eigenvalues is equal to the trace of b_{ij}, which is identically zero by definition; thus, the tensor has only two independent eigenvalues, (λ_1, λ_2). Moreover, from Equations (1,2) it can be seen that a diagonal $b_{ij,\text{pcs}}$ corresponds to a diagonal Reynolds stress tensor $\overline{u_i' u_j'}_{\text{pcs}}$. Since the eigenvalues of $\overline{u_i' u_j'}_{\text{pcs}}$ are non-negative by definition and their maximum value is $2k$, none of the eigenvalues of b_{ij} can be smaller than $-1/3$ (corresponding to a vanishing $\overline{u_i' u_j'}_{\text{pcs}}$ in that component), or greater than $2/3$ (corresponding to only one not-vanishing $\overline{u_i' u_j'}_{\text{pcs}}$ component). Combining the information of two independent eigenvalues with these constraints, it is possible to define two-dimensional maps, where any turbulent state is represented by a point in a bounded region.

The barycentric map, used in this paper and proposed by Banerjee *et al.* (2007), is represented by an equilateral triangle, whose vertices correspond to the three limiting states of the turbulent stress tensor: a one-component limit (1c) with one eigenvalue much larger than the other two, a two-component limit (2c) with two eigenvalues of comparable magnitude, much larger than the third eigenvalue, and a three-component limit (3c) corresponding to the isotropic case with three equal eigenvalues. Eigenvalues can also be called component-energies (Lumley, 1987, p. 131), because they relate to the TKE distribution, and the map shows the shape of the energy ellipsoid associated with the turbulent stress tensor. It is important to stress that this shape is not the shape of the turbulent structures in physical space: one-component turbulence is not a turbulent eddy with a cigar-like (one-dimensional) spatial structure, but with a cigar-like energy ellipsoid, whereas two-component turbulence is not a pancake-like (two-dimensional) spatial eddy, but a turbulent eddy with a pancake-like energy ellipsoid. The Reynolds stress tensor carries only information on componentiality (i.e., the relative strength of different velocity fluctuations in the pcs) not on dimensionality (i.e., the relative uniformity of structures in different directions), which can be studied with other one-point tensors (Kassinos *et al.*, 2001). Moreover, componentality is defined in the pcs; thus, it is not straightforward to relate measured velocity variances and limiting states of anisotropy. This would be possible only if the measured Reynolds stress tensor is diagonal, because principal axes would coincide with those of the reference system used.

To plot a point inside the barycentric map, corresponding to a specific Reynolds stress tensor, barycentric coordinates (x_B, y_B) have to be computed from the two independent and largest eigenvalues λ_1, λ_2 of b_{ij}:

$$\begin{aligned} C_{1\text{c}} &= (\lambda_1 - \lambda_2) \quad C_{2\text{c}} = 2(2\lambda_2 + \lambda_1), \\ C_{3\text{c}} &= (1 - 3\lambda_1 - 3\lambda_2), \\ x_\text{B} &= C_{1\text{c}}x_{1\text{c}} + C_{2\text{c}}x_{2\text{c}} + C_{3\text{c}}x_{3\text{c}}, \\ y_\text{B} &= C_{1\text{c}}y_{1\text{c}} + C_{2\text{c}}y_{2\text{c}} + C_{3\text{c}}y_{3\text{c}}, \end{aligned} \tag{3}$$

where $(x_{i\text{c}}, y_{i\text{c}})$ are the coordinates of the limiting states located at the vertices of the equilateral triangle and can be arbitrarily chosen. In this paper we chose to have the two-component axisymmetric limit in the origin of the coordinate system, with $(x_{2\text{c}}, y_{2\text{c}}) = (0, 0)$, $(x_{1\text{c}}, y_{1\text{c}}) = (1, 0)$, and $(x_{3\text{c}}, y_{3\text{c}}) = (1/2, \sqrt{3}/2)$ (Figure 3). The map has the advantage that every point is associated with a triplet $C_{1\text{c}}, C_{2\text{c}}, C_{3\text{c}}$ that quantifies the contribution of each limiting state of anisotropy to that particular state of the tensor. The centre represents turbulence with an equal contribution of the three limiting states, and any vertex has only one non-zero contribution equal to 1, decreasing to zero on the side opposite to that vertex. As summarised in Banerjee *et al.*, (2007, sec. 2.4), many types of two-dimensional maps with different boundary lines can be constructed to characterise the anisotropy of the Reynolds stress tensor. They are all based on the eigenvalues or invariants of the tensor,

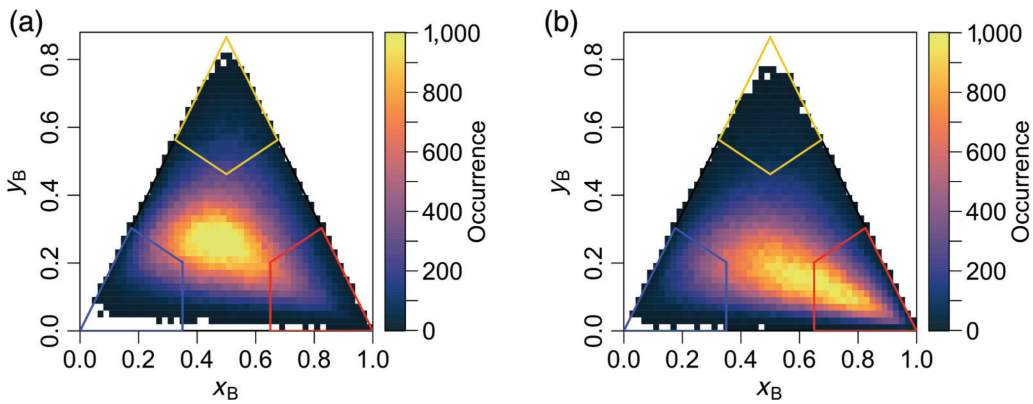

FIGURE 3 Barycentric maps with the occurrence of all ~1 min Reynolds stresses computed from measurements from the 12 sonic anemometers. Right, left and top kite-shaped regions correspond to the area selected as one-component turbulence, two-component axisymmetric turbulence, and isotropic turbulence (Stiperski and Calaf, 2018). (a) The occurrence of the Reynolds stress tensors computed by linear detrending the data before computation of stresses. (b) The occurrence without applying a linear detrending procedure [Colour figure can be viewed at wileyonlinelibrary.com]

and thus not dependent on the frame of reference in which the Reynolds stress tensor is measured. In this paper, the barycentric map is adopted because it avoids visual distortions occurring in other maps, such as visual impression of axisymmetry for turbulent flows that fall in the centre of the barycentric map (Banerjee *et al.*, 2007, fig. 5); thus, it is the most suitable map to investigate Reynolds stress tensors towards the one-component limit, which is commonly observed in the SBL (Vercauteren *et al.*, 2019a). We adopt this map to investigate anisotropy of turbulent eddies within the SnoHATS dataset and we mainly focus on the pure anisotropic states, following the method suggested by Stiperski and Calaf, (2018, fig. 4). Pure states are determined as those periods falling inside the kite-shaped regions of the barycentric map, as shown in Figure 3. The limiting lines were chosen to cover 70% of the sides of the equilateral triangle, with the left region representing Reynolds stress tensors towards the two-component state, the right region those towards the one-component limit, and the upper region those towards the isotropic state.

3.1.1 | Effects of linear detrending

The Reynolds averaging method to estimate turbulent statistics should be applied to steady-state conditions, which are rarely encountered in the atmosphere. The diurnal cycle and/or changes in meteorological conditions may contaminate the turbulent signal with trends, adding low-frequency contributions. It is then common to remove the long-term trends, which are generally approximated as linear. It is up to the investigator to choose the length of the measurement period and whether or not detrending should be used, but it is generally applied to windows of 30 min (Forrer and Rotach, 1997) or more (Foken, 2008). Detrending of shorter time windows may remove part of the turbulent energy in the calculated statistics, and it is a disputed point of turbulence data analysis (Večenaj and Wekker, 2015). The influence of non-stationarity can also be reduced by decreasing the size of the window, and previous studies in the SBL have shown that averaging times shorter than a few minutes often correspond to the observed co-spectral gap that separates turbulence and larger scale processes (Vickers and Mahrt, 2003).

Linear detrending is not frequently applied to 1 min (or few minutes) time windows (Mahrt *et al.*, 1998; Sun *et al.*, 2012; Mahrt *et al.*, 2020; Boyko and Vercauteren, 2021), but it was found to strongly influence the anisotropy analysis of the Reynolds stress tensor in our study. Figure 3 shows the two-dimensional probability density distribution of points in the barycentric map for data subjected (Figure 3a) or not (Figure 3b) to this procedure. In particular, detrending the data reduces the amount of periods falling towards the one-component limit. As the existence of a trend may be interpreted as non-stationarity within the observed time interval, our results are in agreement with Stiperski and Calaf (2018), who found that the amount of one-component stresses is strongly reduced when non-stationary night-time counter-gradient fluxes are discarded from the analysis. The detrending procedure mainly tends to move periods towards the centre of the triangle, where turbulence has an equal mix of the three limiting states, but there are also a few detrended periods that come closer to the one-component limit.

Since we are interested in evaluating the anisotropy of turbulence, we chose to apply the detrending procedure even to this small time window, in order to avoid including this specific contribution from non-stationary external forcings in the components of the Reynolds stress tensor. We will explore linear trends and their sources as a physical reason for one-component anisotropy in Section 4.5.

3.2 | Energy transfer across scales: Coarse-graining approach

In order to investigate the hypothesis that an inverse cascade of kinetic energy may occur in the SBL, according to the state of anisotropy of the Reynolds stress tensor, we employ a coarse-graining approach, commonly used as a modelling tool by the LES community for subgrid-scale processes (Pope, 2000, chap. 13). This approach allows a direct computation of subfilter contributions from highly resolved fields, such as the ones measured during the SnoHATS campaign, and testing the assumptions of LES, in order to improve subgrid scale parametrisations. For example, Bou-Zeid *et al.* (2010) used the SnoHATS dataset to investigate the effects of different filter scales and the role of thermal stability on the coefficients of the Smagorinsky model, when the filter scale is not supposed to be in the inertial subrange of the turbulence spectrum. Many other field campaigns were performed in the atmospheric surface layer for similar purposes: the Davis99 experiment (Porté-Agel *et al.*, 2001), the HATS experiment (Horst *et al.*, 2004), SLTEST (Carper and Porté-Agel, 2004), and SGS2002 (Higgins *et al.*, 2007). However, this approach is very general, and when applied to compute the kinetic energy of the unresolved scales it may be interpreted as a tool to study the energy transfer across scales, and this is the way we use this approach in this paper. Unlike Kolmogorov theory, this method does not rely on assumptions and can assess the direction of the energy flux directly, in contrast to the usual spectral analysis where the same power-law scaling may have multiple interpretations, as in the case of the −3 slope found in Stiperski and Calaf, 2018 or the long-standing debate about the synoptic-to-mesoscale transition (Callies *et al.*, 2014).

The method is exactly derived from the equations governing the conservation of mass and momentum by applying a filtering operator to the atmospheric fields, which leads to the following equations:

$$\begin{aligned} \frac{\partial \tilde{u}_i}{\partial t} + \frac{\partial \tilde{u}_i \tilde{u}_j}{\partial x_j} &= -\frac{1}{\rho}\frac{\partial \tilde{p}}{\partial x_i} - \delta_{i3}\frac{\tilde{\theta} - \langle\tilde{\theta}\rangle}{\tilde{\theta}_0} g \\ &\quad + \nu \frac{\partial^2 \tilde{u}_i}{\partial x_j \partial x_j} - \frac{\partial(\widetilde{u_i u_j} - \tilde{u}_i \tilde{u}_j)}{\partial x_j} \\ \frac{\partial \tilde{u}_i}{\partial x_i} &= 0, \end{aligned} \tag{4}$$

where buoyancy effects are accounted under the Boussinesq approximation, with the angle brackets used to represent a horizontal average (Carper and Porté-Agel, 2004). The filtered field $(\tilde{.})$ is obtained by a convolution of the original field with a function $G_\Delta(\vec{x})$, defined on a compact support or with fast decay, which is normalised and has a characteristic width Δ. In the Fourier space it corresponds to a low-pass filter of cut-off wave number $k_c = \pi/\Delta$. This filtering operation allows a decomposition of the flow to be obtained locally, both in space and time, at any desired scale Δ. The kinetic energy of scales larger than Δ is defined as $\mathrm{KE}^\Delta = \frac{1}{2}\tilde{u}_i\tilde{u}_i$, and its evolution in time can be derived by taking the dot product of Equation (4) with $\tilde{u}_i$:

$$\begin{aligned} \frac{\partial \mathrm{KE}^\Delta}{\partial t} + \tilde{u}_j \frac{\partial \mathrm{KE}^\Delta}{\partial x_j} &= -\frac{1}{\rho}\tilde{u}_i \frac{\partial \tilde{p}}{\partial x_i} - \tilde{u}_3 \frac{\tilde{\theta} - \langle\tilde{\theta}\rangle}{\tilde{\theta}_0} g + \nu \tilde{u}_i \frac{\partial^2 \tilde{u}_i}{\partial x_j \partial x_j} \\ &\quad - \tilde{u}_i \frac{\partial \tau_{ij}}{\partial x_j}, \end{aligned} \tag{5}$$

where $\tau_{ij} = \widetilde{u_i u_j} - \tilde{u}_i \tilde{u}_j$ is the subgrid stress term. The last term on the right-hand side can be written as

$$\begin{aligned} \tilde{u}_i \frac{\partial \tau_{ij}}{\partial x_j} &= \frac{\partial \tilde{u}_i \tau_{ij}}{\partial x_j} - \tau_{ij}\frac{\partial \tilde{u}_i}{\partial x_j} = \frac{\partial \tilde{u}_i \tau_{ij}}{\partial x_j} - \tau_{ij}\frac{1}{2}\left(\frac{\partial \tilde{u}_j}{\partial x_i} + \frac{\partial \tilde{u}_i}{\partial x_j}\right) \\ &= \frac{\partial \tilde{u}_i \tau_{ij}}{\partial x_j} - \tau_{ij}\tilde{S}_{ij}, \end{aligned} \tag{6}$$

where $\tilde{S}_{ij}$ is the resolved strain rate tensor.

The inertial contribution, $\Pi^\Delta = -\tau_{ij}\tilde{S}_{ij}$, corresponds to the rate at which kinetic energy is transferred, by the nonlinear term, from motions of size larger than Δ to motions of smaller size, with positive (negative) values corresponding to a forward (backward) transfer of energy. This term is usually called subgrid-scale dissipation by the LES community. However, this terminology is inappropriate because, unlike the true dissipation, Π^Δ is due entirely to inviscid, inertial processes and it can be negative (Pope, 2000, sec. 13.3.3). In fact, whereas the value of Π^Δ is positive on average, DNS of isotropic turbulence (Domaradzki *et al.*, 1993), as well as studies about LES parametrisations in the atmospheric surface layer based on field measurements (Carper and Porté-Agel, 2004), suggest that, locally, backscatter contributes significantly to the overall transfer of energy across the filter scale, and it should be suitably represented in models to yield correct flow statistics. Boussinesq eddy-viscosity models are absolutely dissipative (unless negative eddy viscosities are allowed), and backscatter is generally included in models by adding nonlinear contributions to the relation between the subgrid stress tensor τ_{ij} and the resolved strain rate tensor $\tilde{S}_{ij}$ (Kosović, 1997). Backscatter of energy is generally associated with the formation of large, coherent structures in the flow field (Carper and Porté-Agel, 2004), and in this paper, through Π^Δ, we investigate if it can also be related to different turbulent topologies, according to the state of anisotropy of the Reynolds stress tensor, driven by strong thermal stratification. Such a coarse graining approach based on Π^Δ was recently used to characterise the energy transfer in the hurricane boundary layer from aircraft measurements (Sroka and Guimond, 2021) and to map out the energy pathways in the North Atlantic Ocean from simulated global ocean data (Aluie *et al.*, 2018).

To compute Π^Δ, we follow the procedure applied by Bou-Zeid *et al.* (2010) to the SnoHATS dataset, where the tilde in Equation (6) corresponds to a two-dimensional horizontal spatial filter, whereas no filtering is applied in the vertical direction. The filtering operation is separately applied to four groups of five sonics each – as summarised by the scheme in Bou-Zeid *et al.* (2010, fig. 2a) – and consists, first, of a box filter of size Δ in the spanwise direction (which is simply the spatial average of the five measured fields in each group) and, second, a Gaussian filter in the streamwise direction. Taylor's hypothesis is invoked to convert time series to streamwise spatial series, and the second filtering operation is applied in the wave-number space, thus taking the product of the Fourier transform of the four (box-filtered) time series with $G(k_1) = \frac{1}{24}\exp(-\Delta^2 k_1^2)$, where k_1 is the streamwise wave number. Taylor's hypothesis may not be appropriate for the most stable regimes, but it is commonly used also in the SBL owing to the lack of a better alternative. Possible inaccuracies mainly concern smaller eddies in the inertial subrange, as it is suggested that they are advected at lower velocities than the mean wind speed (Cheng *et al.*, 2017), and submeso motions, which might not be transported by the local flow (Lang *et al.*, 2018; Pfister *et al.*, 2021). We do not expect these issues to critically influence our results, as we applied the hypothesis to short enough windows, with an averaging time of ~1 min. The characteristic width Δ of the box filter is not simply the spatial distance (4×0.8 m) between the five sonic anemometers in each group. As explained in Carper and Porté-Agel, (2004, fig. 1b), a factor $\cos\delta$, with δ the angle between the direction of the mean wind and the direction perpendicular to the horizontal arrays of sensors, has to be included in order to account for the true separation between neighbouring sensors in the spanwise direction. Thus, $\Delta = 4 \times 0.8\ \mathrm{m} \times \cos\delta$, and according to our restriction on wind direction, described in Section 2, $\Delta_{\min} = 1.6$ m and $\Delta_{\max} = 3.2$ m, with 90% of data in the range [2.2 m, 3.2 m]. The same width Δ is used to define the Gaussian filter in the streamwise direction, and these values of Δ are the smallest achievable with the SnoHATS set-up, if the same spatial resolution is required in both horizontal directions.

Filtered fields are then available at four points (P1, P2, P3, P4), and streamwise, spanwise, and vertical derivatives are obtained at point P2 by finite differences, as summarised by the scheme in Bou-Zeid *et al.* (2010, fig. 2b).

3.3 | Internal gravity waves: Cross-spectral analysis

Key ingredients of stably stratified turbulence are wave-like motions (Mahrt, 2014), such as dirty waves, solitary waves (which are characterised by a single cycle), or IGWs, which may be generated by several mechanisms, including topographic forcing, dynamical instabilities (i.e., shear instability, microfronts or mesoscale fronts), and wave–wave interactions (Staquet and Sommeria, 2002). They manifest as fluctuations in the velocity, pressure, and temperature fields. Different methods may be used to separate IGWs from turbulent motions (Sun *et al.*, 2015a) to properly filter out wavy oscillations, which may lead to turbulent flux overestimation (Cava *et al.*, 2015). In this paper we apply a simple diagnostic method, since our goal is to identify the existence of waves and investigate their influence on the anisotropy of the Reynolds stress tensor at small scales. Our approach is based on linear wave theory (Stull, 1988), which provides most of our understanding of waves. Although it ignores turbulence and irreversible interactions between background flows and waves, it is found to approximately capture the important wave characteristics (such as wave periods, wavelengths, and phase velocity), even for observed nonlinear waves (Sun *et al.*, 2015b, sec. 2.1).

Linear wave theory predicts a phase shift of $\pm 90°$ between the time series of vertical velocity and scalars for gravity-wave events (Stewart, 1969). Thus, the wave-related heat flux $w''\theta''$ (where the double prime denotes wave perturbations with respect to the mean field) would be zero when averaged over an integer number of wave periods. The individual components u'' and w'', instead, are $\pm 180°$ out of phase; thus, linear waves can transport momentum vertically but cannot transport heat or other scalars. The portion of any spectrum composed of linear IGWs can be identified using cross-spectral techniques, which determine the relationship between the two time series, in our case vertical velocity and temperature, as a function of the frequency. From the Fourier transform of their cross-correlation, the real part defines the co-spectrum $\mathrm{Co}_{w\theta}(f)$, whose integral represents the covariance, and the imaginary part defines the quadrature spectrum $Q_{w\theta}(f)$, which is equal to the spectrum of the product of w and θ phase shifted by 90°. The phase spectrum can be constructed from $\mathrm{Co}_{w\theta}(f)$ and $Q_{w\theta}(f)$, generally averaged over similar periods, as

$$\mathrm{Ph}_{w\theta}(f) = \arctan\left(\frac{Q_{w\theta}(f)}{\mathrm{Co}_{w\theta}(f)}\right), \quad (7)$$

where $\mathrm{Ph}_{w\theta}$ represents the average phase difference between w and θ that yields the greatest correlation at each frequency. IGWs and turbulence have different cross-spectral phase signatures: frequencies characterised by IGWs are identified by a phase shift of ±90°, whereas turbulence, being a chaotic motion, has phase angles randomly distributed between −180° and +180°. This difference provides a method to discriminate IGWs from turbulence, which is widely used in the SBL (Rees *et al.*, 2000; Ohya and Uchida, 2003; Cava *et al.*, 2004; Zeri and Sá, 2011; Cava *et al.*, 2015). In this paper, cross-spectral analysis is applied to ∼14 min periods, motivated by the typical wavelengths of IGWs in the SBL. These periods are classified according to the anisotropy of the Reynolds stress tensors at ∼1 min, in order to investigate whether Reynolds stresses towards the one-component limit may be related to the contribution of IGWs. A period is labelled as one- or two-component if at least 50% of the included 1 min periods belongs to that particular state of anisotropy, as further explained in Section 4.4.

4 | RESULTS

4.1 | Anisotropy of the Reynolds stress tensor

Turbulence in a stratified shear layer exhibits significant anisotropy both at large and small scales (Piccirillo and Atta, 1997; Smyth and Moum, 2000; Lang and Waite, 2019). Figure 4 shows the distribution of the three limiting states of anisotropy according to different scales, obtained changing the data window from $2^{10} \sim 1$ min to $2^{15} \sim 30$ min. Anisotropy of the Reynolds stress tensor may be affected by many external parameters, and it is difficult to quantify the influence of each of them. Here, we focus on stratification and wind speed, and we do not separate data according to the height above snow level. However, previous studies Vercauteren *et al.* (2019a, fig. 7), with measurements spanning from 1 m to 30 m a.g.l., have shown an almost constant percentage of one-component states with height, which is the limiting state of anisotropy mainly addressed in this paper. We use data from all sonic anemometers and we classify them into periods of weak wind speed ($\overline{u} \leq 3.5\,\mathrm{m{\cdot}s^{-1}}$, Figure 4a) and strong wind speed ($\overline{u} > 3.5\,\mathrm{m{\cdot}s^{-1}}$, Figure 4b). Figure 4b shows that two-component axisymmetric Reynolds stress tensors are the most frequent for large wind speed, regardless of the window size investigated. However, they become increasingly more common with the longer time-averaging period, which is also the case in the low wind-speed regime (Figure 4a). As suggested by Ali *et al.*, 2018 and Chowdhuri *et al.*, 2020, this may be related to lower wall-normal velocity compared with the horizontal velocity components in larger structures, constrained by their interaction with the surface. The percentage of eddies in the one-component edge is very different for the two cases, with a negligible occurrence at large wind speed, decreasing with the size of eddies (Figure 4b). For low wind speed (Figure 4a), instead, the percentage of one-component Reynolds stress tensor is almost constant, prevailing over two-component anisotropy at the smallest scale. It is interesting to note that, even close to the ground, isotropic eddies can exist

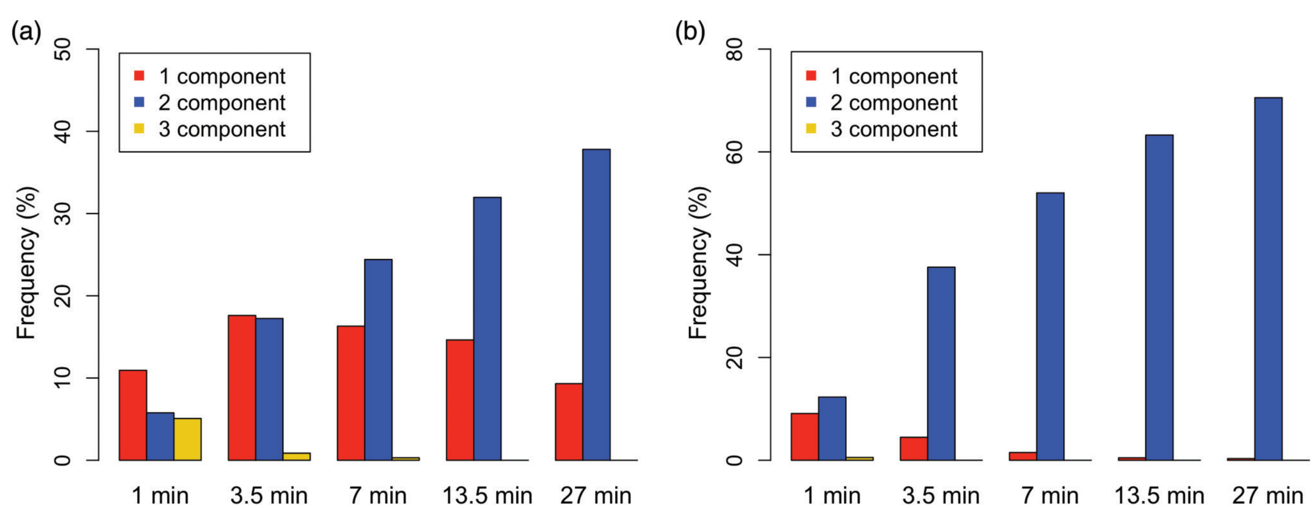

FIGURE 4 Barplots showing the percentage of Reynolds stress tensors in different limiting states of anisotropy, as defined by the edges in Figure 3. Each group corresponds to a different time-averaging period: (a) periods with $\overline{u} \leq 3.5\,\mathrm{m{\cdot}s^{-1}}$; (b) periods with $\overline{u} > 3.5\,\mathrm{m{\cdot}s^{-1}}$ [Colour figure can be viewed at wileyonlinelibrary.com]

at the smallest scales at low wind speed. This seems to be typical of the decoupled SBL, where local shear-generated eddies are too small to interact with the ground directly (Sun *et al.*, 2012), and thus TKE is distributed more uniformly in the three components. Multi-resolution flux decomposition (MRD; Vickers and Mahrt (2003)) analysis shows that the co-spectral gap scale depends on the wind speed regime (not shown), but most of the turbulent transport occurs at scales below ∼1 min even for large wind speed. Thus, the following analysis is based on ∼1 min averaging windows, which minimise the contamination from non-turbulent motions for weak-wind stable conditions. In strong-wind conditions, on the one hand, this choice may discard a small part of turbulent contributions to the Reynolds stress tensor due to larger eddies; however, their contribution would always be towards the two-component axisymmetric limit (Figure 4b). On the other hand, additional one-component states are included in the analysis, but we do not expect them to significantly influence the results.

As shown in Figure 3a, mixed states of anisotropy (i.e., towards the middle of the barycentric map) are the most common ones, in agreement with the results of Vercauteren *et al.* (2019a). They also found a different distribution of the anisotropic limiting states for dynamic regimes classified according to submeso activity, showing that ∼1 min one-component stresses are the most frequent when submeso scales are most active. This is generally the case of the decoupled SBL. Figure 5a shows the distribution of the three limiting states of anisotropy according to the mean wind speed, in order to explore their relation with the SBL regimes' classification provided by Sun *et al.* (2012). Each time average is computed from the measurements of a specific sonic anemometer and results from the analysis of data from all sonic anemometers are then collected together. Whereas Stiperski and Calaf (2018) did not find any correlation between anisotropy and the wind-speed regime when working with 1 min time averages, our analysis suggests that around a wind speed of 3.5 m·s^{-1} there is a change in turbulence topology, corresponding also to a change in mean flow quantities (Figure 5b), which led us to define this value as a threshold wind velocity $\overline{u}_{\mathrm{th}}$. Isotropic eddies only occur under low wind speed, and the transition also influences the relative occurrence of one- and two-component axisymmetric eddies. Whereas below the threshold value the one-component eddies in each wind speed cluster are more frequent than two-component ones, the opposite is true above the threshold. Most of the one-component eddies (75%) are distributed below the threshold value, whereas two-component eddies are distributed almost equally in both dynamic regimes (53% below $\overline{u}_{\mathrm{th}}$). Looking at the value of the mean wind shear and the Brunt–Vaisala frequency, computed from the measurements of the upper and lower arrays using finite differences and with a reference temperature obtained by averaging over all the instruments at each time step,

$$S^2 = \frac{(\overline{u}_{\mathrm{up}} - \overline{u}_{\mathrm{down}})^2}{(\Delta z)^2}$$

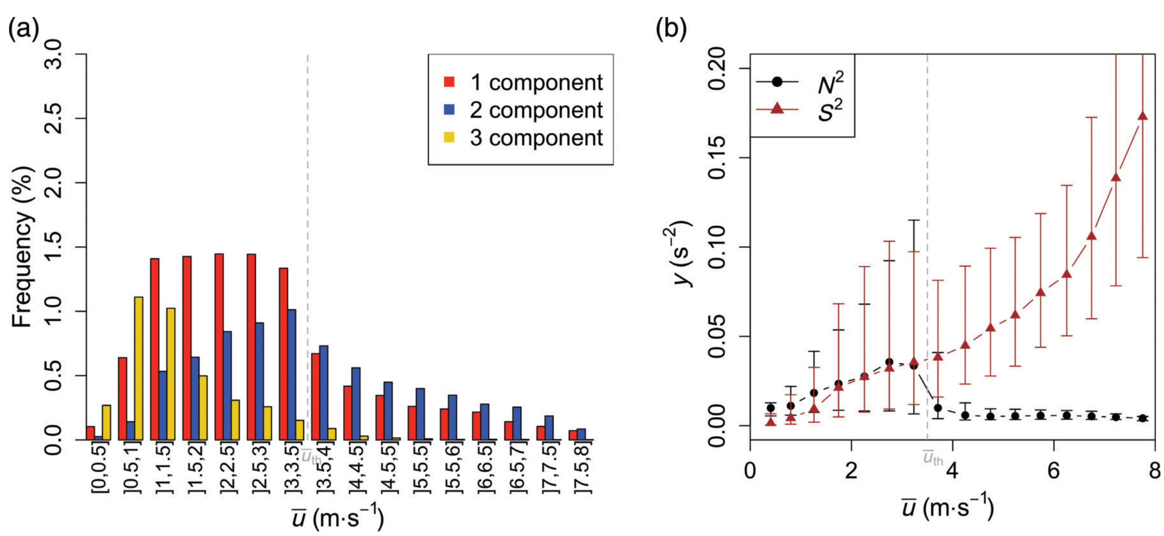

FIGURE 5 (a) Barplot with the percentage of Reynolds stress tensors, with a time-averaging period of ∼1 min, belonging to a particular limiting state of anisotropy, where each group corresponds to a range of mean wind speed. Stresses and mean wind speed are computed for each sonic anemometer and then collected together. (b) The median and the interquartile range (Q_1, Q_3) of the squared Brunt–Vaisala and shear frequencies, computed using finite differences and averaging measurements from the upper and lower arrays of sonics [Colour figure can be viewed at wileyonlinelibrary.com]

and

$$N^2 = \left(\frac{g}{\overline{\theta}}\right)^2 \frac{(\overline{\theta}_{\text{up}} - \overline{\theta}_{\text{down}})^2}{(\Delta z)^2},$$

it is found that the wind-speed threshold separates a regime where local stratification slightly increases with $\overline{u}$ and is comparable to the local wind shear (bulk Richardson number $\text{Ri} = N^2/S^2 \sim 1$) to one dominated by the wind shear.

The increase of N^2 and then its sharp decrease above $\overline{u}_{\text{th}}$ is an interesting feature. The sharp decrease may be understood as a result of turbulent mixing, generated by shear instability as soon as there is enough kinetic energy in the mean flow. The increase in the low-wind speed regime, instead, seems to be associated with katabatic flows. We observed a similar behaviour for stable cases in other datasets collected over a glacier (not shown), but not in datasets collected over flat terrain. For katabatic flows, indeed, we expect an increase in wind speed with thermal stability (Prandtl, 1942), together with a decrease of the jet maximum height, which in turn increases the wind shear. The presence of katabatic flows may then lead to an increasing number of wave-like motions, sometimes observed at the top of drainage currents (Princevac *et al.*, 2008; Viana *et al.*, 2010) and generated by the upward motion of air parcels induced by the irruption of the katabatic flow. Thus, the increase of N^2 may be related also to an increase in wave activity: wave-like motions need a minimum amount of kinetic energy in the mean flow to develop, which is proportional to the mean wind speed, and larger vertical displacements against gravity need larger wind speeds. The increase of N^2 would in turn affect temperature variances, with a larger amount of energy stored into potential energy, as we will see in Section 4.3. There might also be other causes to consider in order to explain this behaviour in the low-wind speed regime, and one working hypothesis we would like to investigate more in future studies is the relation with a general increase in submeso activity with wind speed. Submeso motions may lead to strong temperature anomalies affecting the vertical stratification of the atmospheric layer during their passage. For example, warm submesofronts would increase $\Delta\overline{\theta}$ (Pfister *et al.*, 2021, fig. 5), and they are found to occur preferably for local mean flow with wind speed around $3.5\,\text{m}\cdot\text{s}^{-1}$ (Pfister *et al.*, 2021).

In the clusters with mean wind speed below $1\,\text{m}\cdot\text{s}^{-1}$, where stratification and shear are both low, the occurrence of one-component eddies is still not dominant over the other types, but it increases on approaching the threshold value, after which it decreases sharply, similar to the Brunt–Vaisala frequency. In the following sections, we investigate this relation between strong stability and the occurrence of one-component eddies, how it influences the energy transfer in stratified anisotropic turbulence, and the occurrence of wave–turbulence interaction.

4.2 | Inertial kinetic energy transfer across scales

Thermal stratification over the glacier during the SnoHATS campaign reached values up to $8°\ \text{C}\cdot\text{m}^{-1}$ (Vercauteren and Klein, 2015), which may lead to the horizontal layering of eddies and constrain the flow to a quasi-two-dimensional dynamics. Results obtained by applying the coarse-graining approach described in Section 3.2 at scale Δ are shown in Table 1 and Figure 6. Since the method used to compute the three gradient components evaluates derivatives at the point P2 corresponding to the sonic anemometer at the centre of the lower array, the state of anisotropy of the Reynolds stress tensor is estimated from the measurements taken by this instrument. The backscatter episodes, corresponding to a negative Π^Δ, occur more frequently for one-component stresses than for two-component ones, but the mean energy transfer is always towards smaller scales for both limiting states of anisotropy. The same occurs even when one-component states at large wind speed are not considered. These results led us to reject the hypothesis of the development of two-dimensional turbulence, at least at the scale Δ considered. The mean and the median for the backscatter distribution differ by one order of magnitude, thus showing a strongly asymmetric distribution for both one- and two-component eddies. The former transfers a smaller amount of energy across the scale Δ, both up- and downward. For comparison, the analysis was also performed on the non-detrended dataset (Figure 3b and Table 1). Though the results for two-component eddies are not significantly affected by this change, the results for one-component eddies exhibit appreciable differences. Figure 3 already highlighted the increased representation of one-component stresses without detrending. Here, it is worth noting that there is an increase in the mean backscatter for one-component eddies, whereas the median remains unchanged. The fact that the low-frequency range contributes to the mean backscatter may be attributed to a high correlation between wavelengths in this spectral range, whose interaction leads to backscatter events. It might be argued that, without linearly detrending the data, the fast Fourier transform may suffer from red noise (Stull, 1988) and results may not be reliable. However, the mean forward transfer should be affected in the same way, which does not seem to be the case.

Figure 6 shows the probability density functions of Π^Δ according to one- and two-component Reynolds stresses,

Quarterly Journal of the Royal Meteorological Society RMetS

TABLE 1 Kinetic energy transfers across scale $\Delta \in [1.6\text{ m}, 3.2\text{ m}]$, classified according to the state of anisotropy of the Reynolds stress tensor, with a time-averaging period of ~1 min. Anisotropy is computed from the sonic anemometer at the centre of the lower array; see the text for details about this choice. From left to right: percentage of backscatter events, median of the kinetic energy transfer during backscatter events, mean of the kinetic energy transfer during backscatter and forward transfer events, and percentage of backward energy transfer over the total energy transfer

Anisotropy state	BK events (%)	Median(Π_{BK}) ($m^2 \cdot s^{-3}$)	$\overline{\Pi_{BK}}$ ($m^2 \cdot s^{-3}$)	$\overline{\Pi_{FW}}$ ($m^2 \cdot s^{-3}$)	$\frac{\lvert\overline{\Pi_{BK}}\rvert}{\lvert\overline{\Pi_{BK}}\rvert+\overline{\Pi_{FW}}}$ (%)
One component	34	−0.00023	−0.0065	0.0150	30
Two component	30	−0.00039	−0.0080	0.0217	27
One component (ND)	32	−0.00023	−0.0102	0.0147	41
Two component (ND)	29	−0.00049	−0.0087	0.0206	30

Abbreviations: BK, backscatter; FW, forward transfer; ND, without linear detrending.

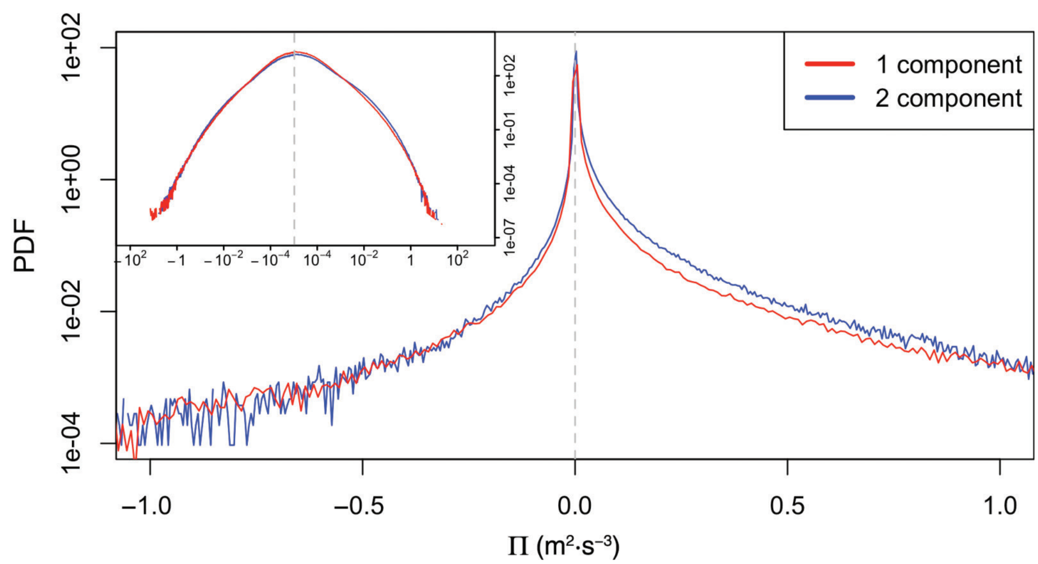

FIGURE 6 Probability density function (PDF) distribution of kinetic energy transfers ($\Pi^{\Delta} = -\tau_{ij}\tilde{S_{ij}}$) across scale $\Delta \in [1.6\text{ m}, 3.2\text{ m}]$ obtained from the measurements of the arrays of sonic anemometers. Each colour corresponds to the probability density distributions computed collecting all ~1 min periods belonging to the same state of anisotropy of the Reynolds stress tensor. Anisotropy is computed from the sonic anemometer at the centre of the lower array (see the text for details about this choice). The inset plot shows the full range of values of Π^{Δ} of the two distributions [Colour figure can be viewed at wileyonlinelibrary.com]

and both distributions are non-Gaussian with heavy tails. Tail asymmetry is large and towards positive values, as expected for a total downward energy transfer, and it is slightly more marked for the two-component cases.

4.3 | Partition of energy between TKE and TPE

In strongly stable night-time conditions, Stiperski and Calaf (2018) found that one-component eddies with 30 min averaging periods generally occur when turbulence destruction by stratification significantly exceeds shear generation in the TKE budget equation. It is now well understood that a negative contribution to the TKE budget due to the buoyancy term may also act as a source term in the TPE budget equation:

$$\mathrm{TPE} = \frac{1}{2}\left(\frac{g}{\Theta_0 N}\right)^2 \overline{\theta'^2}.$$

Thus, a complete description of turbulence in stably stratified atmosphere has to include both turbulent energies (Zilitinkevich *et al.*, 2007; Ďurán *et al.*, 2018). Sun *et al.* (2016) hypothesised that it is the dynamic coupling between TKE and TPE through the buoyancy flux that explains the transition observed at a particular wind-speed threshold in the SBL, as at low wind speed the increase of TKE is limited by the energy consumption for increasing TPE, but at high wind speed this mechanism no longer

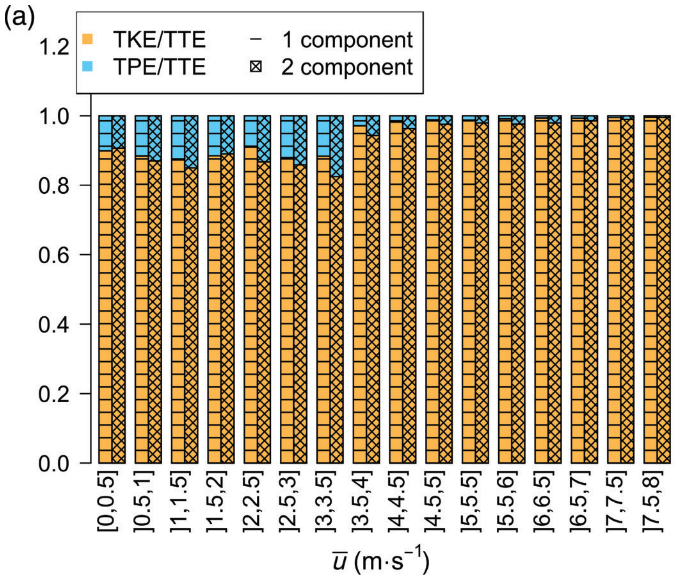

FIGURE 7 Barplots showing the contribution of turbulent potential energy (TPE) and turbulent kinetic energy (TKE) to total turbulence energy (TTE). Each group corresponds to a range of wind speed, and the two bars refer to different limiting states of anisotropy of the Reynolds stress tensor. The time-averaging period is (a) ∼1 min and (b) ∼14 min, and contributions are computed from the medians of TPE and TKE in each cluster [Colour figure can be viewed at wileyonlinelibrary.com]

occurs, leading to a dramatic increase of TKE with wind speed. Motivated by the results of Stiperski and Calaf (2018), we therefore investigated whether this dynamic coupling also implies a particular state of anisotropy of the Reynolds stress tensor.

TPE and TKE were computed for each sonic anemometer and then collected together, according to the state of anisotropy of the Reynolds stress tensor. Contributions of TKE and TPE to the total turbulence energy (TTE), defined as TTE = TKE + TPE, are shown in Figure 7a according to the wind speed, for one- and two-component eddies using ∼1 min time windows. As expected, the low wind-speed regime is characterised by a higher contribution of TPE with respect to the high wind-speed regime, but the two limiting states are comparable, with the TKE contribution being much larger than the TPE one. It is worth noting that the percentage of TPE never exceeds 20%, as was also shown in Kurbatskii and Kurbatskaya (2012, fig. 3) from numerical simulations performed with a RANS model including balance equations for the viscous dissipation ε, TKE, and TPE. These results are in agreement with the energy and flux budget (EFB) turbulence closure in a stably stratified sheared flow (Zilitinkevich *et al.*, 2007), where the TPE is parametrised as a function of the flux Richardson number R_f: TPE = TTE × R_f. Since R_f reaches a maximum asymptotic value of 0.20–0.25, increasing the thermal stability of the mean flow, the EFB theory predicts that the TPE growth is also limited, as validated by LES data and measurements in the laboratory and in the atmosphere (Zilitinkevich *et al.*, 2008, fig. 1).

Extensions of the EFB theory (Zilitinkevich *et al.*, 2009; Kleeorin *et al.*, 2019) showed that the maximum R_f is no longer a universal constant when the contribution of large-scale IGWs is taken into account, but it increases with wave activity, and so does the TPE (Zilitinkevich *et al.*, 2009, fig. 5) for vertically homogeneous stratification (Zilitinkevich *et al.*, 2009, fig. 1). We thus look at longer time windows of ∼14 min, in order to include part of the wave contribution to eddy energetics and seek for possible significant differences between one-component and two-component states. Figure 7b shows that in this case the wind-speed threshold is sharp and one-component periods only occur for low wind speed. At this scale, the contribution of TPE to TTE for one-component periods slightly increases approaching the wind-speed threshold, and it is generally larger than the TPE contribution for the two-component periods. This may be explained by the additional production of TPE by IGWs, thus supporting the hypothesis that one-component Reynolds stress tensors may occur more frequently when there are IGWs. Nevertheless, the maximum percentage of TPE contribution to TTE is still below 25% for every wind speed, which may depend on a low kinetic energy of the wave that can be converted to TPE (Zilitinkevich *et al.*, 2009) or to the close distance to the surface and a dominant contribution of TKE production by the mean shear. In fact, it has been shown by numerical simulations that the TPE contribution increases with height (Maroneze *et al.*, 2019b, fig. 8) and reaches values as high as 90% of TTE for shear-free stably stratified flows (Kleeorin *et al.*, 2019, fig. 11).

As the heat flux plays an essential role in driving SBL regime transitions (Maroneze *et al.*, 2019b), we also checked its dependence on the wind speed, as shown in Figure 8 for one- and two-component ∼1 min Reynolds stresses. Though there is no significant difference in the overall behaviour for the two limiting states of anisotropy, the interquartile range (Q_1, Q_3) of one-component stresses shows that positive heat fluxes may occur below the wind-speed threshold, which is not the case for two-component stresses. The temperature gradient is positive for all the cases considered; thus, a positive flux implies a counter-gradient contribution. In very stable conditions with weak vertical velocity variance, positive heat fluxes may happen because of the dominant contribution of the temperature variance term in the heat flux budget equation, which is always positive and may be driven also by horizontal temperature gradients. Since TPE is proportional to this term, the dominant mechanism in one-component stresses with counter-gradient heat fluxes is the conversion of TPE into TKE and not vice versa, because positive heat fluxes will contribute as a source term in the TKE budget equation and a sink term in the budget equation for temperature variance. In the literature, counter-gradient heat fluxes have been observed for waves strongly interacting with turbulence (Einaudi and Finnigan, 1993; Sun *et al.*, 2015a). Vercauteren *et al.*, (2019a, fig. 8) showed that counter-gradient heat fluxes in the SBL occur more frequently with one-component turbulence, even if they are not always present, concluding that it is not possible to uniquely relate one-component states to counter-gradient heat fluxes, and thus waves. Analogous results are observed here, as the averaged heat flux for all one-component periods is still negative, but with possibility of counter-gradient episodes for low wind speed.

The separation of internal waves from turbulence is still a vexing problem, and generally a fixed time-averaging period is adopted in eddy-covariance analysis. This fixed period might directly include contributions from waves in some cases but not in others; for example, depending on thermal stratification, which influences the period of IGWs. Waves can produce large errors in sign and magnitude of the computed turbulent fluxes, and waves of different periods impact the turbulence statistics and flux calculations differently (Durden *et al.*, 2013; Cava *et al.*, 2015). Since only wave time-scales are characterised by counter-gradient heat fluxes, our results and those from Vercauteren *et al.* (2019a) might also be interpreted as follows. The 1 min periods with counter-gradient heat fluxes are mostly including wave contributions in turbulent statistics, and 1 min one-component periods may or may not include this contribution; thus, not all one-component periods have a counter-gradient heat flux. Nevertheless, it

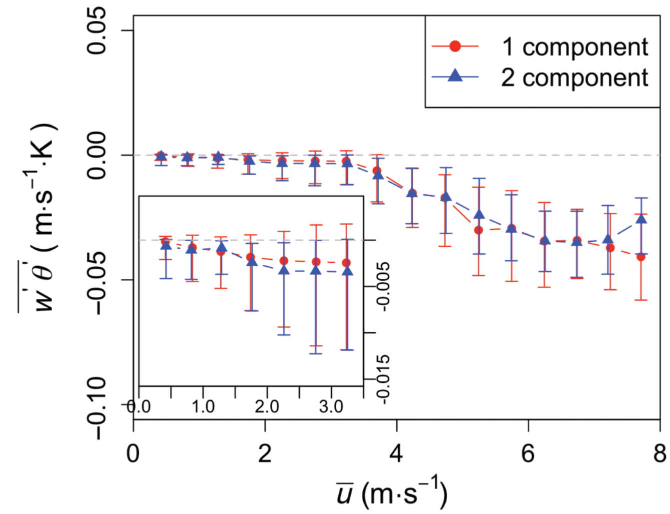

FIGURE 8 Dependence of the heat flux on the mean wind speed, with a time-averaging period of ∼1 min. Data from individual sonic anemometers are analysed separately and then binned together. Points correspond to the median for each range of wind speed, with the bar showing the interquartile range (Q_1, Q_3). The inner plot is a zoom in the low wind-speed regime [Colour figure can be viewed at wileyonlinelibrary.com]

is still possible that IGWs influence the anisotropy of the Reynolds stress tensor at smaller scales (as in the case of wave flume experiments), even if their contribution is not directly included in turbulent statistics, thus relating all one-component periods to waves. Therefore, we proceed in the analysis by further exploring this possibility and working on longer periods of data, classified according to the anisotropy of shorter periods.

4.4 | Linear IGWs and 1 min Reynolds stress tensor

Typical periods of IGWs in the SBL range from 1 to about 10 min (Rees *et al.*, 2001; Sun *et al.*, 2004; Durden *et al.*, 2013; Cava *et al.*, 2015; Zaitseva *et al.*, 2018). In order to study the influence of IGWs on the anisotropy of turbulence, we selected data windows of about 14 min (2^{14} data points), so that the cross-spectral analysis covers the whole range of typical IGW frequencies. The resolved bandwidth then spans from 0.0013 to 10 Hz. Only continuous periods of data were used to select the windows, thus reducing the equivalent of 14 × 24 hr of data to 8 × 24 hr. Each window includes 16 short-time averages of 2^{10} data points (∼1 min time average), which are linearly detrended before computing the Reynolds stress tensor, used to classify periods according to the state of anisotropy. As there are no 16 consecutive 1 min averages with the same type of anisotropy, a criterion to label periods as

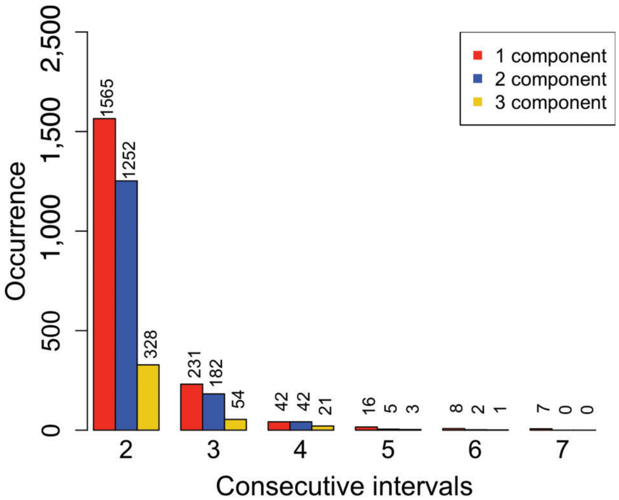

FIGURE 9 Barplot showing the occurrence of periods including consecutive intervals (~1 min time average) with the same state of anisotropy of the Reynolds stress tensor. Each group corresponds to a number of consecutive intervals, and there are no periods including more than seven consecutive intervals with the same state of anisotropy. Data from individual sonic anemometers are analysed separately and then collected together [Colour figure can be viewed at wileyonlinelibrary.com]

one- or two-component had to be chosen. Figure 9 in fact shows that over all the selected data from all the sonic anemometers there are at most seven consecutive 1 min windows whose anisotropy is classified as one-component limit and six for the two-component limit. Turbulence in the same limiting state generally persists for only two consecutive 1 min periods, and then the occurrence decreases sharply for more consecutive intervals. We thus chose to label a 14 min period as one- or two-component if at least 50% of the included 1 min time averages belongs to that particular state of anisotropy. This was a compromise between having enough periods to perform ensemble averages for the cross-spectral analysis and having enough short-time averages to properly associate a period with a well-defined 1 min anisotropy. The method selects a total of 34 one-component 14 min periods for the lower array and 16 for the upper array, including mostly low wind-speed one-component (~80%, not shown). For the two-component periods, there is a big difference in the amount of 14 min periods selected for the two arrays, with just three periods for the upper array and 36 for the lower one. This is in agreement with the increasing occurrence of two-component periods presented in Figure 4 at larger time windows and explained by a stronger interaction of eddies with the ground. In fact, it is expected that, at a fixed time scale, as done here, eddies closer to the surface interact more with the ground than eddies at higher levels do, thus leading to a larger number of periods in the two-component edge. The barycentric map of the 1 min anisotropy for the selected 14 min periods is shown in Figure 10. The spread of the one-component distribution (characterised by 800 short windows) is much larger than for the two-component distribution (characterised by 624 short windows), and the anisotropy of turbulence is closer to the limiting state. The example of a period selected by the method is shown in Figure 11, where Figure 11a (Figure 11b) shows the wind speed and temperature time series for a period classified as one- (two-)component, with the background strips identifying the short time averages with that type of anisotropy.

In Figure 11a, a wavelike pattern, highlighted by an ellipse, can be recognised from minutes 9 to 11 in the temperature time series, with a wave period shorter than the averaging time window used to compute turbulent stresses. Similar patterns are not easily identified by visual inspection in the two-component case in Figure 11b.

Following the cross-spectral method explained in Section 3.3, we computed the median co-spectra and quadrature spectra for the 50 one-component and 39 two-component periods, with the former shown in Figure 12a. Frequencies are normalised by the mean wind speed, according to Taylor's hypothesis, and are made dimensionless with measurement height. At each scale, both one- and two-component periods contribute negatively to the heat flux, but two-component periods have larger negative values because eddies of this type are characterised by larger wind speed (Figure 5a), leading to stronger turbulence production. The corresponding phase spectra with the interquartile range (Q_1, Q_3) are shown in Figure 12b in absolute value. For IGWs, a ±90° phase angle is expected at the wave frequency. One-component periods, which we hypothesised to be more influenced by IGWs, show a tendency towards larger absolute phase shifts at large scales. The fact that there is not exactly a tendency towards 90° might be due to the analysis considering all one-component periods together, without a further classification. Waves of different frequencies or not pure linear waves and contributions from other types of submeso motions are hence considered together, thus smoothing out the phase signal when the median is taken. Nevertheless, a clearly distinct behaviour can be recognised according to anisotropy, with the two-component periods having smaller phase shifts with respect to the one-component ones at larger scales. Instead, they have a similar behaviour at the smallest scales, where the effect of IGWs is not expected to be important. There is, thus, evidence that periods characterised by one-component anisotropy at smaller scales may be related to IGWs at larger scales. To further investigate this relationship, we proceed in the next section with a complementary

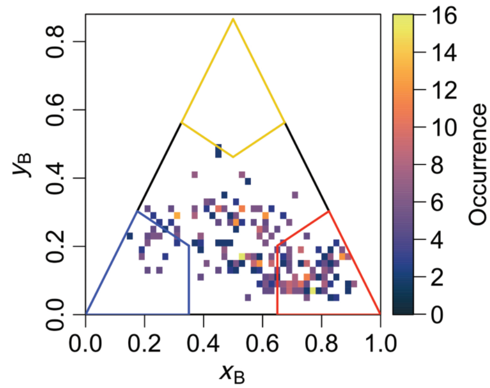

FIGURE 10 Barycentric maps with the occurrence of all short periods of ~1 min, included in the 14 min periods used in the cross spectral analysis. One- (two-)component periods include at least eight ~1 min Reynolds stresses in the one- (two-)component state. (a) The barycentric map for the 50 one-component periods; (b) the barycentric map for the 39 two-component periods [Colour figure can be viewed at wileyonlinelibrary.com]

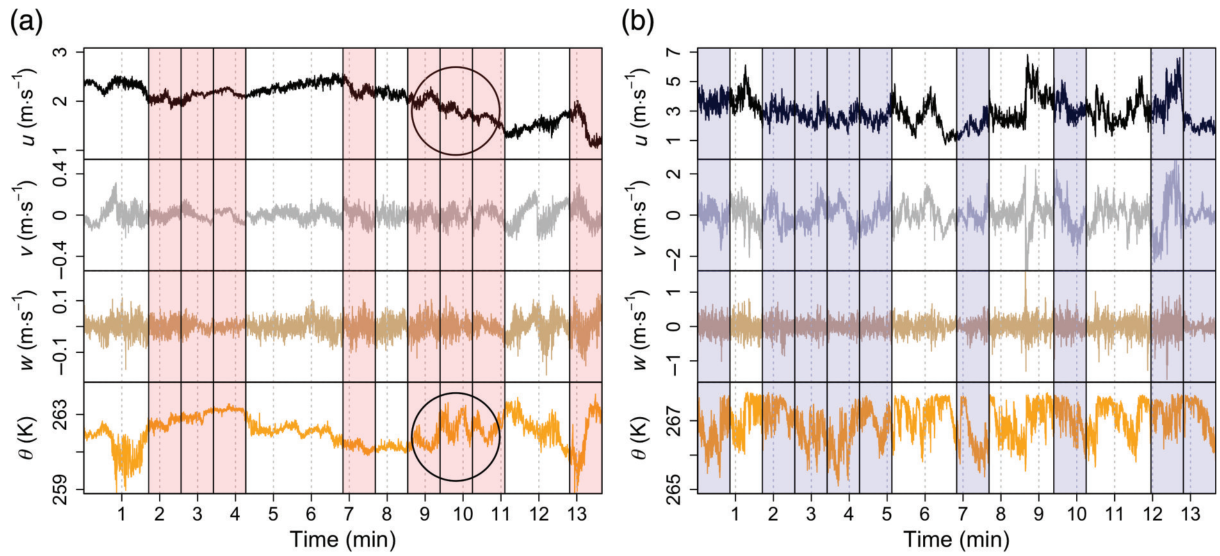

FIGURE 11 Wind speed (double rotated) and temperature time series extracted from the measurements of the central sonic anemometer in the bottom array. (a) Time series for a period classified as one-component: February 2, 2006, from 00:57:38 to 01:11:24. (b) Time series for a period classified as two-component: April 17, 2006, from 02:51:14 to 03:05:10. In each period the background strips identifies the 1 min time windows classified as one (panel a) and two component (panel b) [Colour figure can be viewed at wileyonlinelibrary.com]

analysis: Given a detected wave, what is the corresponding anisotropy of the Reynolds stress tensor at small scales?

4.5 | Anisotropy analysis of a clean wave

In order to answer the aforementioned question, we need observations of a wave whose characteristics are as close as possible to ideal conditions. These are found for waves with oscillations of approximately constant amplitude and period, also referred to as clean waves (Sun *et al.*, 2015a). Clean waves are uncommon and were not detected in the SnoHATS campaign; thus, only for this analysis, we use a different dataset from a field campaign over a flat site in Dumosa (−35.868304° S, 143.343323° E), Australia (Lang *et al.*, 2018; Mahrt *et al.*, 2021). Figure 13a shows the time series of wind speed, temperature, and pressure in a window selected from measurements at 3 m a.g.l. collected by a sonic anemometer at a frequency of 10 Hz. The MRD technique is used to determine the appropriate averaging period for the anisotropy analysis of turbulent scales and, as shown in Figure 13b, the co-spectral gap is found around 1 min, and thus 2^9 data windows are selected (marked by red lines in Figure 13a). The double-rotation method is applied to data, as done for the previous analyses. A wave

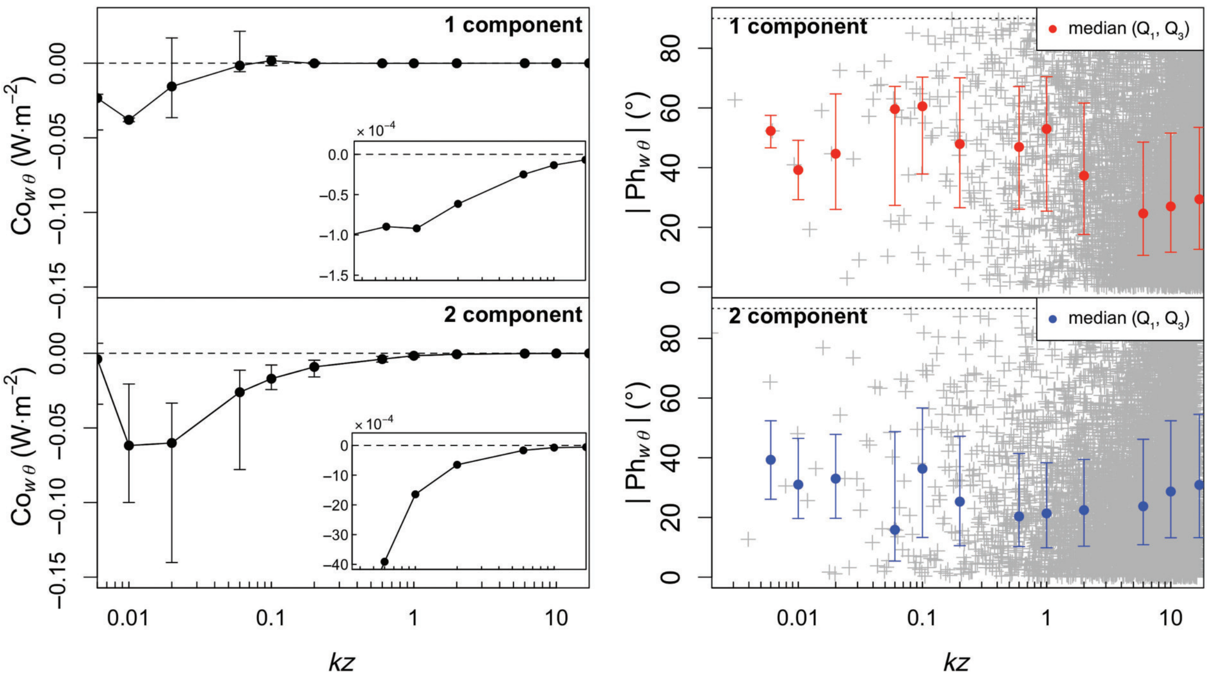

FIGURE 12 Cross-spectral analysis of vertical velocity and temperature for 14 min periods, with one- (two-)component periods including at least eight ~1 min Reynolds stresses in the one- (two-)component state. (a) The median per bin of normalised frequencies of the median co-spectrum over all the individual 14 min periods (50 one-component periods and 39 two-component periods) and the corresponding interquartile range (Q_1, Q_3), with the inset plot zooming into the high-frequency range. (b) The corresponding phase spectrum in absolute value and the interquartile range (Q_1, Q_3), with individual data points shown in grey [Colour figure can be viewed at wileyonlinelibrary.com]

with a period of around 6 min (~0.003 Hz) is observed for half an hour during the night between 1557 UTC and 1633 UTC and consists of few cycles with decreasing amplitude. The wave period corresponds well to the second peak observed in the MRD co-spectrum at $\tau = 409$ s, thus showing that even this clean wave is not purely monochromatic, as most waves encountered in the atmosphere, and therefore the total wave-heat flux could be different from the zero value prescribed by the linear wave theory. The observed wave seems to be generated by the passage of a microfront, as the temperature time-series exhibits a sharp increase of about 2 K in 3 min, characterised also by small quasi-periodic fluctuations. This is an interesting feature, as it corroborates the hypothesis previously presented in Section 4.1 that the increase of atmospheric stability with mean wind speed in the decoupled SBL may be related to microfronts, which, as shown here, can in turn imply wave activity. The barycentric coordinates, Equation (3), of the full window (2^{15} data) are close to the one-component limit with $(x_B, y_B) = (0.89, 0.02)$, and the same occurs if the interval is decreased to ~7 min (closer to the period of the observed wave), with six out of eight windows falling in the one-component edge (not shown). One-component states are observed throughout the wave event when the interval is further decreased to ~1 min, except at the wave peaks, where two-component states occur due to the enhancement of the wind shear by the wave itself, as shown in Figure 13a by the background strips, respectively.

It follows that a wave contributes to drive the Reynolds stress tensor towards the one-component limit in two ways: if many (or at least one) wave cycles are included in the time interval or if just the fraction of the wave cycle corresponding to the trend in the time series is included. The latter contribution can be a priori removed in those turbulence studies interested in limiting the effects of low-frequency (submeso) contributions to turbulence statistics. Figure 13c, indeed, shows that a linear detrending method is sufficient to move the one-component Reynolds stress tensors towards the centre of the barycentric map. However, this method is effective on waves with periods larger than the averaging interval, whereas all the others will still contribute to drive the Reynolds stress tensor towards the one-component limit. The wavelike pattern identified in the time series in Figure 11a shows exactly that, with windows labelled as one-component during the passage of a wave with a period shorter than ~1 min. From this wave analysis, it follows that Reynolds stresses towards the one-component limit may include non-turbulent contributions from waves, which should be considered as a spurious contribution if we are only interested in turbulence characteristics.

Quarterly Journal of the Royal Meteorological Society RMetS

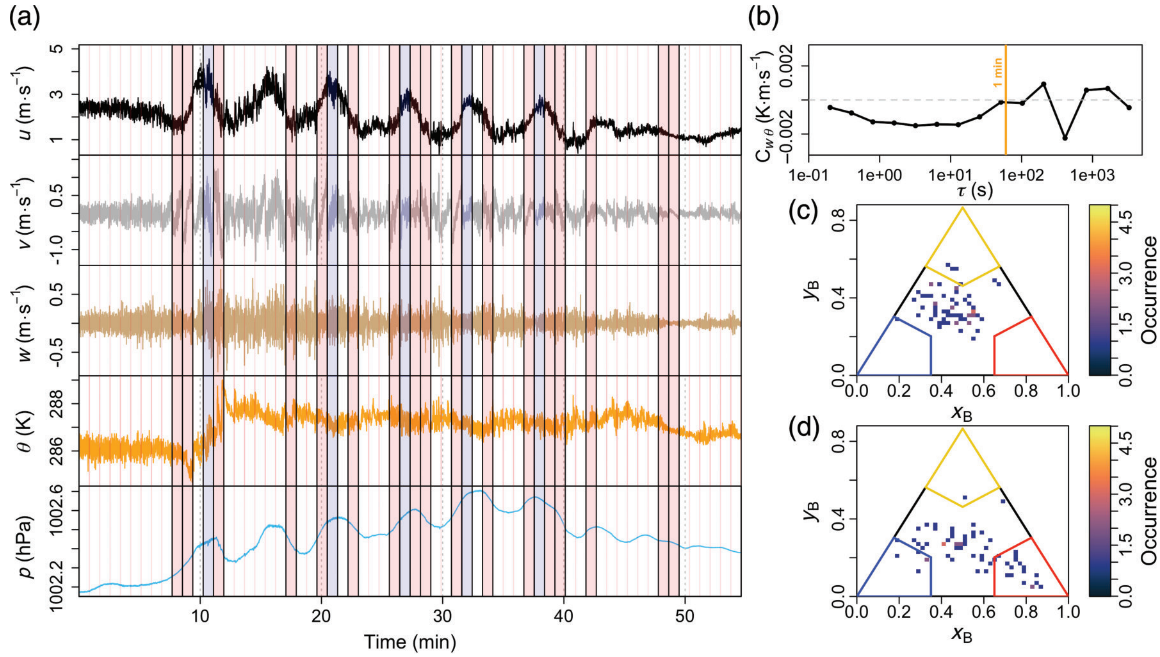

FIGURE 13 Analysis of a wave observed in Dumosa, Australia. Panel (a) shows the wind speed (double-rotated), temperature and pressure time series, with light lines delimiting each time window. The background strips identifies the 1-min time windows classified according to limiting state of anisotropy. Panel (b) shows the heat flux MRD cospectrum, while panel (c) and panel (d) show the corresponding barycentric maps with the occurrence of Reynolds stresses, computed applying (c) or not (d) a linear detrending procedure to individual periods [Colour figure can be viewed at wileyonlinelibrary.com]

5 | CONCLUSIONS

The study presented in this article examined the shape of the Reynolds stress tensor in the SBL. The SnoHATS dataset, collected over a glacier at the height of about 2 m a.g.l., was used for the analysis, and the frequent occurrence of one-component states under strongly stably stratified conditions was investigated, in relation to two hypotheses. One is that strong temperature stratification may enable the development of quasi-two-dimensional dynamics, as suggested by the formation of horizontal layers observed in stratified turbulent flow, and thus lead to two-dimensional turbulence, characterised by an inverse energy cascade. The other hypothesis is that IGWs, ubiquitous in the SBL, may influence the shape of the Reynolds stress tensor at small scale, contributing to the one-component cases, and may lead to a different distribution of turbulent energy into kinetic and potential energy.

Vercauteren *et al.* (2019a) already observed frequent occurrence of one-component Reynolds stresses in the SBL and attributed it to a non-stationary interaction between submeso motions and turbulence scales. Our findings suggest that these non-stationary forcings may introduce trends in the time window used to compute turbulence (1 min is mainly adopted in this study) and that those trends lead the small-scale contribution to the Reynolds stress tensor towards the one-component limit. Nevertheless, after linear trend removal, we found that one-component states still dominate the low wind-speed regime, characterised by strong stratification. The three limiting states of anisotropy (isotropic, two-component, and one-component) show a clear relation to wind speed, suggesting a wind-speed threshold $\overline{u_{\mathrm{th}}}$ of about 3.5 m·s^{-1}. Isotropic and one-component states occur almost exclusively below $\overline{u_{\mathrm{th}}}$, whereas larger wind speeds are mainly connected with two-component states. The latter start to become more frequent than one-component states when the threshold wind speed is crossed, and they dominate the high wind-speed regime especially if time averages larger than 1 min are adopted. The change in turbulence topology between two-component and isotropic/one-component states is found to be related to a change in the relative contribution of local static stability and wind shear. Though larger wind speed implies larger wind shear close to the surface, this does not lead to an increasing occurrence of isotropic turbulence. This seems related to the fact that shear-generated turbulent eddies at large wind speed are coupled with the surface, and the straining effect due to shear leads energy to be distributed along two dominant directions. At low wind speed, instead, isotropic eddies may be produced by localised weak shears, related to submeso activity, and they are decoupled from the surface, with TKE distributed more uniformly in three directions. This interpretation is in agreement with Vercauteren *et al.* (2019a, fig. 7), where the proportion of isotropic stresses was found to increase with distance above the ground, whereas that of two-component was found to decrease.

By quantifying the energy exchange between large and small scales, our findings do not support the hypothesis that one-component turbulence is related to two-dimensional turbulence. The backward mean kinetic energy transfer was always smaller than the forward energy transfer, about half of it at the scale $\Delta = 3.2$ m considered. Analogous results were obtained for two-component cases, with no significant difference in the energy exchange across scales between these two types of anisotropic stresses.

On the other hand, our results show that waves play an important role in modulating anisotropy at small time averages towards the one-component limit. Investigation of 14 min periods with dominant 1 min one-component and 1 min two-component states showed that the phase shifts between temperature and vertical velocity in the low-frequency range were larger (close to 60°) for one-component than for two-component spectra. At larger scales, a possible wave signature was also found in 14 min Reynolds stress tensors towards the one-component limit at low wind speed, as they were characterised by an increasing contribution of potential energy to the total energy of the fluctuations, following the behaviour of local stability. Further evidence for the role of waves in one-component turbulence was obtained by analysing a clean wave signal measured at 3 m a.g.l. in Dumosa (Australia). The Reynolds stress tensor of a complete wave cycle has a one-component signature, as well as the Reynolds stress tensor of an approximately linear trend caused by sampling only a fraction of the wave cycle. A wavelet representation based on MRD for heat fluxes does not remove such trends; thus, the turbulence time-scale estimated from MRD co-spectra may include non-turbulent contributions to the Reynolds stress tensor. For those SBL studies interested in limiting the effect of submeso motions on turbulence statistics, such contributions are spurious and we recommend to apply the MRD technique together with a linear detrending procedure. The influence of trends is a specific case supporting the general understanding that non-stationary interaction between submeso motions and turbulence scales may drive one-component Reynolds stress tensors. It also suggests that the existence of trends in measured velocity variances leads to one-component Reynolds stress tensors, because TKE is mainly distributed along the direction of the submeso forcing. However, a key point in tensor analysis of anisotropy is that the off-diagonal terms of the Reynolds stress tensor matter, which is why a direct link between measured velocity variances (dependent on the coordinate system) and component energies (eigenvalues, independent of the coordinate system) is not straightforward, unless the measured Reynolds stress tensor is almost diagonal. In this specific case, the coordinate system used would coincide with the principal component coordinate system. This is not usually the case, and the observed one-component stresses seem to be also characterised by large $\overline{u'v'}$ (Stiperski *et al.*, 2021, fig. S1a, supplemental material). It would be interesting for a future study to extract different types of submeso motions (Kang *et al.*, 2014; 2015; Vercauteren *et al.*, 2019b) and analyse their contribution to the anisotropy of the Reynolds stress tensor. For example, it is known that meandering motions may lead to tendencies in the spanwise and streamwise velocity variance, but their specific contribution to anisotropy still has to be explored.

Our results thus support the idea that, for improving turbulence modelling in the decoupled regime of the SBL, a necessary step is to include wave forcing. A promising technique is to combine recent approaches based on potential/kinetic energy conversion processes and on the anisotropy of the Reynolds stress tensor.

AUTHOR CONTRIBUTIONS

Federica Gucci: conceptualization; formal analysis; methodology; software; visualization; writing – original draft. **Lorenzo Giovannini:** methodology; supervision; writing – review and editing. **Ivana Stiperski:** methodology; software; writing – review and editing. **Dino Zardi:** methodology; supervision; writing – review and editing. **Nikki Vercauteren:** conceptualization; methodology; software; supervision; writing – review and editing.

ACKNOWLEDGEMENTS

We thank the EFLUM laboratory at EPFL for providing the SnoHATS data and Danijel Belušić for providing the Dumosa data, as well as two anonymous reviewers for their valuable comments. F. Gucci is grateful to Marco Falocchi for introducing her to the anisotropy analysis of the Reynolds stress tensor, and to Sergej Zilitinkevich for inspiring discussions about turbulence in the SBL. We thank the organisers of the winter school "Physics and Mathematics of Turbulent Flows at Different Scales", which took place between February 24 and March 1, 2019, at the Les Houches School of Physics based in Les Houches, France, to make this collaboration possible. The work of I. Stiperski was funded by the Austrian Science Fund (FWF) grant T781-N32. N. Vercauteren and F. Gucci thank the University of Oslo for starter pack funds that covered part of the work. F. Gucci also thanks the University of Trento for supporting funds to spend a research period at the Freie Universität Berlin, where part of the work has been done.

CONFLICT OF INTEREST

The authors declare no conflict of interest.

ORCID

Federica Gucci https://orcid.org/0000-0003-3583-9765
Lorenzo Giovannini https://orcid.org/0000-0003-1650-0344
Ivana Stiperski https://orcid.org/0000-0003-2154-6603
Dino Zardi https://orcid.org/0000-0002-3573-3920
Nikki Vercauteren https://orcid.org/0000-0003-2893-9186

REFERENCES

Acevedo, O.C., Costa, F.D., Maroneze, R., Carvalho, A.D., Puhales, F.S. and Oliveira, P.E. (2021) External controls on the transition between stable boundary-layer turbulence regimes. *Quarterly Journal of the Royal Meteorological Society*, 147, 2335–2351.

Ali, N., Hamilton, N., Cortina, G., Calaf, M. and Cal, R.B. (2018) Anisotropy stress invariants of thermally stratified wind turbine array boundary layers using large eddy simulations. *Journal of Renewable and Sustainable Energy*, 10, 013301.

Alisse, J.-R. and Sidi, C. (2000) Experimental probability density functions of small-scale fluctuations in the stably stratified atmosphere. *Journal of Fluid Mechanics*, 402, 137–162.

Aluie, H., Hecht, M. and Vallis, G.K. (2018) Mapping the energy cascade in the North Atlantic Ocean: The coarse-graining approach. *Journal of Physical Oceanography*, 48, 225–244.

Atta, C.V. (1991) Local isotropy of the Smallest Scales of Turbulent Scalar and Velocity Fields. *Proceedings: Mathematical and Physical Sciences*, 434, 139–147.

Baas, P., van de Wiel, B.J., van Meijgaard, E., Vignon, E., Genthon, C., van der Linden, S.J. and de Roode, S.R. (2019) Transitions in the wintertime near-surface temperature inversion at Dome C, Antarctica. *Quarterly Journal of the Royal Meteorological Society*, 145, 930–946.

Banerjee, S., Krahl, R., Durst, F. and Zenger, C. (2007) Presentation of anisotropy properties of turbulence, invariants versus eigenvalue approaches. *Journal of Turbulence*, 8, N32.

Bolgiano, R. (1959) Turbulent spectra in a stably stratified atmosphere. *Journal of Geophysical Research*, 64, 2226–2229.

Bou-Zeid, E., Higgins, C., Huwald, H., Meneveau, C. and Parlange, M.B. (2010) Field study of the dynamics and modelling of subgrid-scale turbulence in a stable atmospheric surface layer over a glacier. *Journal of Fluid Mechanics*, 665, 480–515.

Boyko, V. and Vercauteren, N. (2021) Multiscale shear forcing of turbulence in the nocturnal boundary layer: a statistical analysis. *Boundary-Layer Meteorology*, 179, 43–72.

Callies, J., Ferrari, R. and Bühler, O. (2014) Transition from geostrophic turbulence to inertia-gravity waves in the atmospheric energy spectrum. *Proceedings of the National Academy of Sciences of the United States of America*, 111, 17033–17038.

Carper, M.A. and Porté-Agel, F. (2004) The role of coherent structures in subfilter-scale dissipation of turbulence measured in the atmospheric surface layer. *Journal of Turbulence*, 5, 040.

Cava, D., Giostra, U. and Katul, G. (2015) Characteristics of gravity waves over an antarctic ice sheet during an austral summer. *Atmosphere*, 6, 1271–1289.

Cava, D., Giostra, U., Siqueira, M. and Katul, G. (2004) Organised motion and radiative perturbations in the nocturnal canopy sublayer above an even-aged pine forest. *Boundary-Layer Meteorology*, 112, 129–157.

Cheng, Y., Sayde, C., Li, Q., Basara, J., Selker, J., Tanner, E. and Gentine, P. (2017) Failure of taylor's hypothesis in the atmospheric surface layer and its correction for eddy-covariance measurements. *Geophysical Research Letters*, 44, 4287–4295.

Chowdhuri, S., Kumar, S. and Banerjee, T. (2020) Revisiting the role of intermittent heat transport towards Reynolds stress anisotropy in convective turbulence. *Journal of Fluid Mechanics, 899*, A26.

Domaradzki, J.A., Liu, W. and Brachet, M.E. (1993) An analysis of subgrid-scale interactions in numerically isotropic turbulence. *Physics of Fluids*, 5, 1747–1759.

Ďurán, I.B., Geleyn, J.F., Vána, F., Schmidli, J. and Brožková, R. (2018) A turbulence scheme with two prognostic turbulence energies. *Journal of the Atmospheric Sciences*, 75, 3381–3402.

Durden, D.J., Nappo, C.J., Leclerc, M.Y., Duarte, H.F., Zhang, G., Parker, M.J. and Kurzeja, R.J. (2013) On the impact of wave-like disturbances on turbulent fluxes and turbulence statistics in nighttime conditions: a case study. *Biogeosciences*, 10, 8433–8443.

Einaudi, F. and Finnigan, J.J. (1993) Wave-turbulence dynamics in the stably stratified boundary layer. *Journal of Atmospheric Sciences*, 50, 1841–1864.

Emory, M., Larsson, J. and Iaccarino, G. (2013) Modeling of structural uncertainties in Reynolds-averaged Navier-Stokes closures. *Physics of Fluids*, 25, 110822.

Falocchi, M., Giovannini, L., de Franceschi, M. and Zardi, D. (2019) A method to determine the characteristic time-scales of quasi-isotropic surface-layer turbulence over complex terrain: a case-study in the Adige Valley (Italian Alps). *Quarterly Journal of the Royal Meteorological Society*, 145, 495–512.

Finnigan, J.J., Einaudi, F. and Fua, D. (1984) The interaction between an internal gravity wave and turbulence in the stably-stratified nocturnal boundary layer. *Journal of Atmospheric Sciences*, 41, 2409–2436.

Foken, T. (2008) *Micrometeorology*. Berlin, Heidelberg: Springer.

Forrer, J. and Rotach, M.W. (1997) On the turbulence structure in the stable boundary layer over the Greenland ice sheet. *Boundary-Layer Meteorology*, 85, 111–136.

Grachev, A.A., Andreas, E.L., Fairall, C.W., Guest, P.S. and Persson, P.O.G. (2013) The critical richardson number and limits of applicability of local similarity theory in the stable boundary layer. *Boundary-Layer Meteorology*, 147, 51–82.

Harikrishnan, A., Ansorge, C., Klein, R. and Vercauteren, N. (2021) *Geometry and organization of coherent structures in stably stratified atmospheric boundary layers*. http://arxiv.org/abs/2110.02253.

Higgins, C.W., Meneveau, C. and Parlange, M.B. (2007) The effect of filter dimension on the subgrid-scale stress, heat flux, and tensor alignments in the atmospheric surface layer. *Journal of Atmospheric and Oceanic Technology*, 24, 360–375.

Horst, T.W., Kleissl, J., Lenschow, D., Meneveau, C., Moeng, C.-H., Parlange, M., Sullivan, P. and Weil, J. (2004) HATS: field observations to obtain spatially filtered turbulence fields from crosswind arrays of sonic anemometers in the atmospheric surface layer. *Journal of the Atmospheric Sciences*, 61, 1566–1581.

Jofre, L., Domino, S.P. and Iaccarino, G. (2018) A framework for characterizing structural uncertainty in large-eddy simulation closures. *Flow, Turbulence and Combustion*, 100, 341–363.

Kang, Y., Belušić, D. and Smith-Miles, K. (2014) Detecting and classifying events in noisy time series. *Journal of the Atmospheric Sciences*, 71, 1090–1104.

Kang, Y., Belušić, D. and Smith-Miles, K. (2015) Classes of structures in the stable atmospheric boundary layer. *Quarterly Journal of the Royal Meteorological Society*, 141, 2057–2069.

Kassinos, S.C., Reynolds, W.C. and Rogers, M.M. (2001) One-point turbulence structure tensors. *Journal of Fluid Mechanics*, 428, 213–248.

Katul, G.G., Parlange, M.B., Albertson, J.D. and Chu, C.R. (1995) Local isotropy and anisotropy in the sheared and heated atmospheric surface layer. *Boundary Layer Meteorology*, 72, 123–148.

Kit, E., Barami, E. and Fernando, H.J.S. (2021) Structure functions in nocturnal atmospheric boundary layer turbulence. *Physical Review Fluids*, 6, 084605.

Kleeorin, N., Rogachevskii, I., Soustova, I.A., Troitskaya, Y.I., Ermakova, O.S. and Zilitinkevich, S. (2019) Internal gravity waves in the energy and flux budget turbulence-closure theory for shear-free stably stratified flows. *Physical Review E*, 99, 063106.

Kolmogorov, A. (1941) The local structure of turbulence in incompressible viscous fluid for very large reynolds numbers. *Doklady Akademii Nauk SSSR*, 30, 301–304.

Kosović, B. (1997) Subgrid-scale modelling for the large-eddy simulation of high-Reynolds-number boundary layers. *Journal of Fluid Mechanics*, 336, 151–182.

Kurbatskii, A.F. and Kurbatskaya, L.I. (2012) On the eddy mixing and energetics of turbulence in a stable atmospheric boundary layer. *Izvestiya - Atmospheric and Ocean Physics*, 48, 595–602.

Lang, C.J. and Waite, M.L. (2019) Scale-dependent anisotropy in forced stratified turbulence. *Physical Review Fluids*, 4, 044801.

Lang, F., Belušić, D. and Siems, S. (2018) Observations of wind-direction variability in the nocturnal boundary layer. *Boundary-Layer Meteorology*, 166, 51–68.

Longo, S., Clavero, M., Chiapponi, L. and Losada, M.A. (2017) Invariants of turbulence reynolds stress and of dissipation tensors in regular breaking waves. *Water*, 9, 893.

Lovejoy, S. and Schertzer, D. (2013) *The weather and climate: emergent laws and multifractal cascades*. Cambridge Press University.

Lovejoy, S., Schertzer, D., Silas, P., Tessier, Y. and Lavallé e, D. (1993) The unified scaling model of atmospheric dynamics and systematic analysis of scale invariance in cloud radiances. *Geophysicae*, 11, 119–127.

Lumley, J.L. (1987) Computational modeling of turbulent flows. *Advances in Applied Mechanics*, 18, 123–176.

Mahrt, L. (2014) Stably stratified atmospheric boundary layers. *Annual Review of Fluid Mechanics*, 46, 23–45.

Mahrt, L., Belušić, D. and Acevedo, O. (2021) Small-scale spatial variation of the nocturnal wind field. *Boundary-Layer Meteorology*, 180, 225–245.

Mahrt, L., Pfister, L. and Thomas, C.K. (2020) Small-scale variability in the nocturnal boundary layer. *Boundary-Layer Meteorology*, 174, 81–98.

Mahrt, L., Sun, J., Blumen, W., Delany, T. and Oncley, S. (1998) Nocturnal boundary-layer regimes. *Boundary-Layer Meteorology*, 88, 255–278.

Mahrt, L., Sun, J. and Stauffer, D. (2015) Dependence of turbulent velocities on wind speed and stratification. *Boundary-Layer Meteorology*, 155, 55–71.

Maroneze, R., Acevedo, O.C., Costa, F.D., Puhales, F.S., Demarco, G. and Mortarini, L. (2019a) The nocturnal boundary layer transition from weakly to very stable. Part II: numerical simulation with a second-order model. *Quarterly Journal of the Royal Meteorological Society*, 145, 3593–3608.

Maroneze, R., Acevedo, O.C., Costa, F.D. and Sun, J. (2019b) Simulating the regime transition of the stable boundary layer using different simplified models. *Boundary-Layer Meteorology*, 170, 305–321.

Mishra, A.A., Mukhopadhaya, J., Alonso, J. and Iaccarino, G. (2020) Design exploration and optimization under uncertainty. *Physics of Fluids*, 32, 085106.

Oettl, D., Goulart, A., Degrazia, G. and Anfossi, D. (2005) A new hypothesis on meandering atmospheric flows in low wind speed conditions. *Atmospheric Environment*, 39, 1739–1748.

Ohya, Y. and Uchida, T. (2003) Turbulence structure of stable boundary layers with a near-linear temperature profile. *Boundary-Layer Meteorology*, 108, 19–38.

Pfister, L., Lapo, K., Mahrt, L. and Thomas, C.K. (2021) Thermal submesoscale motions in the nocturnal stable boundary layer. Part 1: detection and mean statistics. *Boundary-Layer Meteorology*, 180, 187–202.

Piccirillo, P. and Atta, C.W.V. (1997) The evolution of a uniformly sheared thermally stratified turbulent flow. *Journal of Fluid Mechanics*, 334, 61–86.

Pope, S.B. (2000) *Turbulent Flows*. Cambridge University Press.

Porté-Agel, F., Parlange, M.B., Meneveau, C. and Eichinger, W.E. (2001) A priori field study of the subgrid-scale heat fluxes and dissipation in the atmospheric surface layer. *Journal of the Atmospheric Sciences*, 58, 2673–2698.

Prandtl, L. (1942) *Führer durch die Strömungslehre*. Vieweg und Sohn: Braunschweig, Germany.

Princevac, M., Hunt, J.C.R. and Fernando, H.J.S. (2008) Quasi-steady katabatic winds on slopes in wide valleys: hydraulic theory and observations. *Journal of the Atmospheric Sciences*, 65, 627–643.

Rees, J.M., Denholm-Price, J.C.W., King, J.C. and Anderson, P.S. (2000) A climatological study of internal gravity waves in the atmospheric boundary layer overlying the brunt ice shelf, antarctica. *Journal of the Atmospheric Sciences*, 57, 511–526.

Rees, J.M., Staszewski, W.J. and Winkler, J.R. (2001) Case study of a wave event in the stable atmospheric boundary layer overlying an Antarctic Ice Shelf using the orthogonal wavelet transform. *Dynamics of Atmospheres and Oceans*, 34, 245–261.

Sagaut, P. and Cambon, C. (2018) *Homogeneous turbulence dynamics*. Springer International Publishing AG.

Schertzer, D. and Lovejoy, S. (1985) *The Dimension and Intermittency of Atmospheric Dynamics. In: Turbulent Shear Flows 4*, (pp. 7–33). Berlin, Heidelberg: Springer Berlin Heidelberg.

Singh, S.K., Raushan, P.K., Kumar, P. and Debnath, K. (2021) Anisotropy of reynolds stress tensor in combined wave-current flow. *Journal of Offshore Mechanics and Arctic Engineering*, 143, 051202.

Smyth, W.D. and Moum, J.N. (2000) Anisotropy of turbulence in stably stratified mixing layers. *Physics of Fluids*, 12, 1343–1362.

Sroka, S. and Guimond, S.R. (2021) Organized kinetic energy backscatter in the hurricane boundary layer from radar measurements. *Journal of Fluid Mechanics*, 924, A21.

Staquet, C. and Sommeria, J. (2002) Internal gravity waves: from instabilities to turbulence. *Annual Review of Fluid Mechanics*, 34, 559–593.

Stewart, R.W. (1969) Turbulence and waves in a stratified atmosphere. *Radio Science*, 4, 1269–1278.
Stiperski, I. and Calaf, M. (2018) Dependence of near-surface similarity scaling on the anisotropy of atmospheric turbulence. *Quarterly Journal of the Royal Meteorological Society*, 144, 641–657.
Stiperski, I., Katul, G. and Calaf, M. (2021) Universal return to isotropy of inhomogeneous atmospheric boundary layer turbulence. *Physical Review Letters*, 126, 194501.
Stull, R.B. (1988) *An introduction to boundary layer meteorology*. Kluwer Academic Publishers.
Sukoriansky, S. and Galperin, B. (2012) An analytical theory of the buoyancy-Kolmogorov subrange transition in turbulent flows with stable stratication. *Philosophical Transactions of the Royal Society A*, 371, 20120212.
Sun, J., Lenschow, D.H., Burns, S.P., Banta, R.M., Newsom, R.K., Coulter, R., Frasier, S., Ince, T., Nappo, C., Balsley, B.B., Jensen, M., Mahrt, L., Miller, D. and Skelly, B. (2004) Atmospheric disturbances that generate intermittent turbulence in nocturnal boundary layers. *Boundary-Layer Meteorology*, 110, 255–279.
Sun, J., Lenschow, D.H., LeMone, M.A. and Mahrt, L. (2016) The role of large-coherent-eddy transport in the atmospheric surface layer based on CASES-99 observations. *Boundary-Layer Meteorology*, 160, 83–111.
Sun, J., Mahrt, L., Banta, R.M. and Pichugina, Y.L. (2012) Turbulence regimes and turbulence intermittency in the stable boundary layer: during CASES-99. *Journal of the Atmospheric Sciences*, 69, 338–351.
Sun, J., Mahrt, L., Nappo, C. and Lenschow, D.H. (2015a) Wind and temperature oscillations generated by wave-turbulence interactions in the stably stratified boundary layer. *Journal of the Atmospheric Sciences*, 72, 1484–1503.
Sun, J., Nappo, C.J., Mahrt, L., Belušic, D., Grisogono, B., Stauffer, D.R., Pulido, M., Staquet, C., Jiang, Q., Pouquet, A., Yagüe, C., Galperin, B., Smith, R.B., Finnigan, J.J., Mayor, S.D., Svensson, G., Grachev, A.A. and Neff, W.D. (2015b) Review of wave-turbulence interactions in the stable atmospheric boundary layer. *Reviews of Geophysics*, 53, 956–993.
Vallis, G.K. (2005) *Atmospheric and Oceanic Fluid Dynamics*. Cambridge University Press.
Vassilicos, J.C. (2015) Dissipation in turbulent flows. *Annual Review of Fluid Mechanics*, 47, 95–114.
Vercauteren, N., Boyko, V., Faranda, D. and Stiperski, I. (2019a) Scale interactions and anisotropy in stable boundary layers. *Quarterly Journal of the Royal Meteorological Society*, 145, 1799–1813.
Vercauteren, N., Boyko, V., Kaiser, A. and Belušić, D. (2019b) Statistical investigations of flow structures in different regimes of the stable boundary layer. *Boundary-Layer Meteorology*, 173, 143–164.
Vercauteren, N. and Klein, R. (2015) A clustering method to characterize intermittent bursts of turbulence and interaction with submesomotions in the stable boundary layer. *Journal of the Atmospheric Sciences*, 72, 1504–1517.
Vercauteren, N., Mahrt, L. and Klein, R. (2016) Investigation of interactions between scales of motion in the stable boundary layer. *Quarterly Journal of the Royal Meteorological Society*, 142, 2424–2433.
Večenaj, Z. and Wekker, S.F.D. (2015) Determination of non-stationarity in the surface layer during the T-REX experiment. *Quarterly Journal of the Royal Meteorological Society*, 141, 1560–1571.
Viana, S., Terradellas, E. and Yagüe, C. (2010) Analysis of gravity waves generated at the top of a drainage flow. *Journal of the Atmospheric Sciences*, 67, 3949–3966.
Vickers, D. and Mahrt, L. (2003) The cospectral gap and turbulent flux calculations. *Journal of Atmospheric and Oceanic Technology*, 20, 660–672.
Vignon, E., van de Wiel, B.J., van Hooijdonk, I.G., Genthon, C., van der Linden, S.J., van Hooft, J.A., Baas, P., Maurel, W., Traullé, O. and Casasanta, G. (2017) Stable boundary-layer regimes at Dome C, Antarctica: observation and analysis. *Quarterly Journal of the Royal Meteorological Society*, 143, 1241–1253.
Watanabe, T. and Nagata, K. (2021) Large-scale characteristics of a stably stratified turbulent shear layer. *Journal of Fluid Mechanics*, 927, A27.
Watanabe, T., Riley, J.J., Nagata, K., Matsuda, K. and Onishi, R. (2019) Hairpin vortices and highly elongated flow structures in a stably stratified shear layer. *Journal of Fluid Mechanics*, 878, 37–61.
Wingstedt, E.M., Fossum, H.E., Reif, B.A. and Werne, J. (2015) Anisotropy and shear-layer edge dynamics of statistically unsteady, stratified turbulence. *Physics of Fluids*, 27, 065106.
Zaitseva, D.V., Kallistratova, M.A., Lyulyukin, V.S., Kouznetsov, R.D. and Kuznetsov, D.D. (2018) The effect of internal gravity waves on fluctuations in meteorological parameters of the atmospheric boundary layer. *Izvestiya, Atmospheric and Oceanic Physics*, 54, 173–181.
Zeri, M. and Sá, L.D. (2011) Horizontal and Vertical turbulent fluxes forced by a gravity wave event in the nocturnal atmospheric surface layer over the amazon forest. *Boundary-Layer Meteorology*, 138, 413–431.
Zilitinkevich, S., Druzhinin, O., Glazunov, A., Kadantsev, E., Mortikov, E., Repina, I. and Troitskaya, Y. (2019) Dissipation rate of turbulent kinetic energy in stably stratified sheared flows. *Atmospheric Chemistry and Physics*, 19, 2489–2496.
Zilitinkevich, S.S., Elperin, T., Kleeorin, N., L'Vov, V. and Rogachevskii, I. (2009) Energy- and flux-budget turbulence closure model for stably stratified flows. Part II: the role of internal gravity waves. *Boundary-Layer Meteorology*, 133, 139–164.
Zilitinkevich, S.S., Elperin, T., Kleeorin, N. and Rogachevskii, I. (2007) Energy- and flux-budget (EFB) turbulence closure model for stably stratified flows. Part I: steady-state, homogeneous regimes. *Boundary-Layer Meteorology*, 125, 167–191.
Zilitinkevich, S.S., Elperin, T., Kleeorin, N., Rogachevskii, I., Esau, I., Mauritsen, T. and Miles, M.V. (2008) Turbulence energetics in stably stratified geophysical flows: strong and weak mixing regimes. *Quarterly Journal of the Royal Meteorological Society*, 134, 793–799.

How to cite this article: Gucci, F., Giovannini, L., Stiperski, I., Zardi, D. & Vercauteren, N. (2023) Sources of anisotropy in the Reynolds stress tensor in the stable boundary layer. *Quarterly Journal of the Royal Meteorological Society*, 149(750), 277–299. Available from: https://doi.org/10.1002/qj.4407